

# Lecture notes on the physics of cosmic microwave background anisotropies

Anthony Challinor<sup>\*,†</sup> and Hiranya Peiris<sup>\*</sup>

*<sup>\*</sup>Institute of Astronomy and Kavli Institute for Cosmology Cambridge, Madingley Road, Cambridge, CB3 0HA, UK*

*<sup>†</sup>DAMTP, Centre for Mathematical Sciences, Wilberforce Road, Cambridge, CB3 0WA, UK*

**Abstract.** We review the theory of the temperature anisotropy and polarization of the cosmic microwave background (CMB) radiation, and describe what we have learned from current CMB observations. In particular, we discuss how the CMB is being used to provide precise measurements of the composition and geometry of the observable universe, and to constrain the physics of the early universe. We also briefly review the physics of the small-scale CMB fluctuations generated during and after the epoch of reionization, and which are the target of a new breed of arcminute-resolution instruments.

**Keywords:** Cosmic microwave background; cosmic inflation

**PACS:** 98.80.-k; 98.70.Vc

## 1. INTRODUCTION

The last two decades have seen remarkable advances in observational cosmology and quantitative cosmological constraints now come from a number of complementary probes. Amongst these, the cosmic microwave background temperature and polarization anisotropies have played a particularly important role. The physics is very well understood – the primary contribution to the anisotropies is accurately described by linear perturbation theory – and so theoretical predictions are believed to be accurate to better than 1%. Furthermore, the CMB currently provides the most direct observational link to the physics of the early universe since the fluctuations were mostly imprinted around the time of recombination.

The physics of the CMB anisotropies is now a textbook subject [1]. The basic picture is that the angular variations in temperature that we observe today are a snapshot of the local properties (density, peculiar velocity and the total gravitational potential) of the gas of CMB photons at the time the primordial plasma recombined at redshift  $z \approx 1100$ . These quantities are related to the primordial perturbations, plausibly generated during an epoch of cosmological inflation, by the rather simple acoustic physics of the pre-recombination plasma. The CMB anisotropies therefore encode information on the primordial perturbation itself, as well as the matter composition and geometry of the universe. By mapping the microwave sky, cosmologists thus hope to answer some of the biggest questions in physics.

Large-angle temperature anisotropies were first discovered by COBE-DMR in 1992 [2]. Since then, tens of instruments have mapped the anisotropies and we now have high quality measurements of the statistics of the anisotropies over three decades

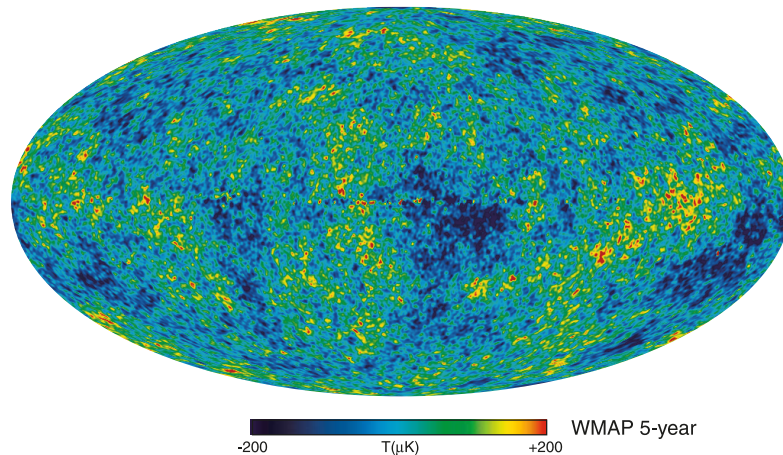


**FIGURE 1.** Fluctuations in the CMB temperature, as determined from five years of WMAP data, about the average temperature of 2.725 K. Reproduced from [3].

of angular scales. The current state-of-the-art dataset is provided by COBE's successor, the WMAP satellite, which released its five-year results in March 2008 [3]. A map of the temperature fluctuations from WMAP, after removing the effect of microwave emission from our galaxy, is shown in Fig. 1. The WMAP results are beautifully fit by a simple cosmological model with flat space, baryons and cold dark matter making up 4% and 21% respectively of the energy density with the remaining 75% in some form of dark energy, and Gaussian-distributed, adiabatic primordial density perturbations with an almost, but not quite, scale-invariant spectrum. The accuracy of these numbers is quite remarkable by cosmological standards; for example, the baryon density is measured to better than 3% and space is flat to better than 1%. Inflation continues to stand up to exacting comparison with observations. Indeed, the quality of the data is now good enough to rule out several popular inflation models from the plethora that theorists have proposed. The community now eagerly awaits the launch of Planck, the third-generation CMB satellite, in mid-2009. This will image the sky in nine wavelength bands with a best resolution below 5 arcmin. Forecasts indicate that Planck should measure several important parameters to better than 1%, and place tight constraints on inflation models [4].

The CMB temperature fluctuations are complemented by its linear polarization [5]. Polarization is generated by scattering of anisotropic radiation and for the CMB this occurs at two epochs: around recombination and, later, from the epoch of reionization [6]. The small polarization signal (r.m.s.  $\sim 5 \mu\text{K}$ ) was first detected in 2002 by the DASI instrument [7], and has subsequently been measured by several groups. The signal-to-noise of these measurements is still poor compared to the temperature anisotropies, but already important constraints have emerged on the epoch of reionization from WMAP [8, 9]. Polarization also provides the only viable route in the near-future for detecting the background of gravitational waves predicted from inflation in models with large, i.e. super-Planckian, field values [10, 11]. A positive detection would be particularly interesting for attempts to realise inflation in string theory, and would rule out some alternatives to inflation such as the cyclic model [12]. Since Planck may not have the sensitivity to

make a definitive test of gravitational waves, a new generation of ambitious sub-orbital instruments that will deploy hundreds or even thousands of superconducting detectors to beat down the noise are under construction. These exciting instruments aim to probe the highly uncertain physics of energies near  $10^{16}$  GeV.

In addition to these *primary* anisotropies, there are a number of *secondary* processes that add further structure to the CMB at late times (see Ref. [13] for a recent review). These include gravitational redshifts induced by the linear evolution of the gravitational potentials once dark energy becomes dynamically important [14], gravitational lensing of CMB photons by the large-scale distribution of matter [15, 16, 17], and various scattering effects that become operative after the onset of reionization [18, 19, 20]. While the observation and interpretation of the primary anisotropies is now a mature field, for the secondary processes, in which the CMB is used as a back-light, this is just beginning. A new breed of instruments with arcminute resolution are now surveying these secondary effects with the hope of improving our understanding of the epoch of reionization and the growth of structure over a wide range of redshifts. If these new observations are to fulfill their scientific potential, accurate modelling of secondary anisotropies is required. This properly requires large numerical simulations and is currently a very active area of CMB theory.

In these lecture notes we outline the basic physics of the primary temperature and polarization anisotropies of the CMB, and discuss how observations of these are being used to constrain cosmological models and the physics of the early universe. For earlier reviews that are similar in spirit, see for example [21, 22, 23]. We also briefly review secondary anisotropies and look forward to what we may learn from the new high-resolution surveys.

## 2. INTRODUCTION TO CMB TEMPERATURE ANISOTROPIES

The CMB radiation has an exquisite blackbody (thermal) spectrum, with very nearly the same temperature of 2.725 K in all directions on the sky [24, 25]. The largest temperature variation is a dipole due to our motion relative to the CMB. Initially, ignore the small effect of the temperature fluctuations due to the primordial perturbations. Then the CMB is isotropic in its rest frame with a Lorentz-invariant distribution function<sup>1</sup>  $\bar{f}(p^\mu) \propto 1/(e^{E_{\text{CMB}}/T_{\text{CMB}}} - 1)$  where  $E_{\text{CMB}}$  is the photon energy in the CMB frame and  $T_{\text{CMB}} = \bar{T}$  is the isotropic temperature. If we observe a photon with energy  $E$  and direction  $\mathbf{e}$ , then the relativistic Doppler shift gives  $E_{\text{CMB}} = E\gamma(1 + \mathbf{v} \cdot \mathbf{e})$ , where  $\mathbf{v}$  is our velocity relative to the CMB. In terms of the energy and direction in our reference frame,

$$\bar{f}(p^\mu) \propto \frac{1}{e^{E\gamma(1+\mathbf{v}\cdot\mathbf{e})/T_{\text{CMB}}} - 1}. \quad (1)$$

This still looks like a blackbody along any direction but the observed temperature varies over the sky as  $T(\mathbf{e}) = T_{\text{CMB}}/[\gamma(1 + \mathbf{v} \cdot \mathbf{e})] \approx T_{\text{CMB}}(1 - \mathbf{v} \cdot \mathbf{e})$  for  $|\mathbf{v}| \ll 1$ , i.e. a dipole anisotropy. The measured dipole [26] implies the solar system barycentre has speed

---

<sup>1</sup> The one-particle distribution function gives the number of photons per proper phase-space volume.

$3.68 \times 10^5 \text{ m s}^{-1}$  relative to the CMB. It is clear from Eq. (1) that relative motion also produces quadrupole anisotropies at  $O(|\mathbf{v}|^2)$  and CMB data is routinely corrected for this (small) effect. Reinstating the contributions of the primordial perturbation to the temperature anisotropies, these are at the level of one part in  $10^5$  and dominate over the relative-velocity effects for the observed quadrupole and higher multipoles.

## 2.1. CMB observables

It is convenient to expand the temperature fluctuation in spherical harmonics,

$$\Delta T(\hat{\mathbf{n}})/\bar{T} = \sum_{lm} T_{lm} Y_{lm}(\hat{\mathbf{n}}), \quad (2)$$

with  $T_{lm}^* = (-1)^m T_{l-m}$  since the temperature is a real field. The sum in Eq. (2) runs over  $l \geq 1$ , but the dipole ( $l = 1$ ) is usually removed explicitly when analysing data since it depends linearly on the velocity of the observer. Multipoles at  $l$  encode angular information with characteristic scale (i.e. period)  $\sim 2\pi/l$ .

The statistical properties of the fluctuations in a perturbed cosmology can be expected to respect the symmetries of the background model. In the case of Robertson-Walker models, this means the *statistics* should be independent of spatial position (homogeneous) and invariant under rotations of the field. Under a rotation specified by Euler angles  $\alpha$ ,  $\beta$  and  $\gamma$ , the  $T_{lm}$  transform to  $\sum_{m'} D_{mm'}^l(\alpha, \beta, \gamma) T_{lm'}$  where  $D_{mm'}^l$  is a Wigner rotation matrix. Demanding invariance under rotations fixes the second-order statistics to be of the form

$$\langle T_{lm} T_{l'm'}^* \rangle = C_l^T \delta_{ll'} \delta_{mm'}, \quad (3)$$

which defines the power spectrum  $C_l^T$ . The angle brackets in this equation denote the average over an ensemble of realisations of the fluctuations. The simplest models of inflation predict that the fluctuations should also be Gaussian at early times, and this is preserved by linear evolution of the small fluctuations. Equation (3) tells us that the  $T_{lm}$  are uncorrelated for different  $l$  and  $m$  and, if Gaussian, they are also independent. In this case, the power spectrum provides the complete statistical description of the temperature anisotropies. For this reason, measuring the anisotropy power spectrum has, so far, been the main goal of observational CMB research.

If we were given ideal (i.e. noise-free) measurements of the temperature over the full sky, the CMB power spectrum could be estimated by

$$\hat{C}_l^T = \frac{1}{2l+1} \sum_m |T_{lm}|^2. \quad (4)$$

This is an unbiased estimator of the true ensemble  $C_l^T$ , but has an irremovable *cosmic variance* due to the finite number  $(2l+1)$  of modes that we can observe. If the temperature anisotropies are Gaussian distributed,  $\hat{C}_l^T$  has a  $\chi^2$  distribution with  $2l+1$  degrees of freedom and the cosmic variance is [27]

$$\text{var}(C_l^T) = \frac{2}{2l+1} (C_l^T)^2. \quad (5)$$

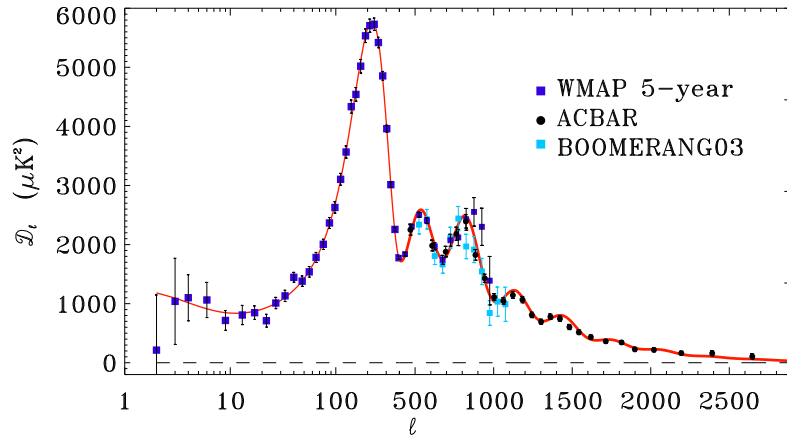


**FIGURE 2.** The temperature anisotropy power spectrum,  $\mathcal{D}_l \equiv l(l+1)C_l^T/(2\pi)$ , as measured by WMAP5 (blue; [29]), ACBAR (black; [30]) and BOOMERanG (cyan; [31]). The line is the best-fit flat,  $\Lambda$ CDM model to the WMAP5 and ACBAR data. Reproduced from [30].

In practice, estimating the power spectrum is complicated by a number of real-world complexities such as partial sky coverage and instrumental noise. The critical review by Efstathiou [28] provides a useful entry point to the large literature on practical methods for estimating the temperature power spectrum.

We show in Fig. 2 a selection of recent measurements of  $C_l^T$  taken from [30]. WMAP and ACBAR are currently the most constraining of all measurements of  $C_l^T$  on large and small scales, respectively, but will be improved upon significantly by Planck for  $l > 500$ . (WMAP5 is cosmic-variance limited to  $l = 530$  [29].) Also shown in Fig. 2 is the theoretical power spectrum for the best-fit flat,  $\Lambda$ CDM model to the WMAP5 and ACBAR data. The agreement is striking, with five acoustic peaks clearly delimited. Moreover, the agreement between different experiments (and technologies) is excellent where they overlap in  $l$  coverage. Understanding the main features in the  $C_l^T$  spectrum is one of the principal aims of these lecture notes.

The correlation between the temperature anisotropies along two directions evaluates to

$$\langle \Delta T(\hat{\mathbf{n}}_1) \Delta T(\hat{\mathbf{n}}_2) \rangle = \bar{T}^2 \sum_l \frac{2l+1}{4\pi} C_l^T P_l(\cos \theta), \quad (6)$$

which depends only on the angular separation  $\theta$  as required by rotational invariance. Here,  $P_l(x)$  are the Legendre polynomials. The mean-square temperature anisotropy is

$$\langle \Delta T^2 \rangle = \bar{T}^2 \sum_l \frac{2l+1}{4\pi} C_l^T \approx \bar{T}^2 \int \frac{l(l+1)}{2\pi} C_l^T d \ln l, \quad (7)$$

so that the quantity  $l(l+1)C_l^T/2\pi$ , which is conventionally plotted, is approximately the power per decade in  $l$  of the temperature anisotropies.

*Higher-Order Statistics.* In Gaussian theories, all higher-order correlations of the  $T_{lm}$  can be reduced to the power spectrum by Wick's theorem. In non-Gaussian theories,

the form of the correlators is restricted by rotational invariance. Here, we shall just consider the three-point function which must take the form

$$\langle T_{l_1 m_1} T_{l_2 m_2} T_{l_3 m_3} \rangle = B_{l_1 l_2 l_3} \begin{pmatrix} l_1 & l_2 & l_3 \\ m_1 & m_2 & m_3 \end{pmatrix}, \quad (8)$$

where the right-hand side involves the Wigner  $3j$  symbol (which enforces  $m_1 + m_2 + m_3 = 0$ ) and the *angular bispectrum*  $B_{l_1 l_2 l_3}$ . If we further assume that the generation and propagation of cosmological perturbations respects parity symmetry, the bispectrum must then vanish for  $l_1 + l_2 + l_3$  odd. Parity invariance further ensures that the bispectrum is real and invariant under arbitrary perturbations of its indices. There is, as yet, no strong evidence for a non-zero CMB bispectrum; see Sec. 5.3.3. For a discussion of the CMB four-point function, or trispectrum, see [32].

## 2.2. Thermal history

The high temperature of the early universe maintained a low equilibrium fraction of neutral atoms, and a correspondingly high number density of free electrons. Coulomb scattering between the ions and electrons kept them in local kinetic equilibrium, and Thomson scattering of photons tended to maintain the isotropy of the CMB in the baryon rest frame. As the universe expanded and cooled, the dominant element hydrogen started to recombine when the temperature fell below  $\sim 4000$  K. This is a factor of 40 lower than might be anticipated from the 13.6-eV ionization potential of hydrogen, and is due to the large ratio of the number of photons to baryons. Through recombination, the mean-free path for Thomson scattering grew to the horizon size and CMB photons “decoupled” from matter. More precisely, the probability density that photons last scattered at some time defines the *visibility function*. This is now known to peak 380 kyr after the big bang [3], with a width  $\sim 120$  kyr. Since then, CMB photons have propagated relatively unimpeded for 13.7 Gyr, covering a comoving distance  $\chi_* = 14.1$  Gpc. The distribution of their energies carries the imprint of fluctuations in the radiation temperature, the gravitational potentials, and the peculiar velocity of the radiation where they last scattered, as the temperature anisotropies that we observe today. Only a small fraction of CMB photons – current results from CMB polarization measurements [9] indicate around 10 per cent – underwent further scattering once the universe reionized, due to the ionizing radiation from the first stars.

The details of hydrogen recombination are complicated since it occurs out of quasi-equilibrium, but the broad details are well understood [33, 34]. Most hydrogen atoms recombined through the (forbidden) two-photon transition between the  $2s$  and  $1s$  states. Direct recombination to  $1s$ , or via allowed transitions from excited states, would have produced a large excess of photons more energetic than Ly- $\alpha$  (i.e. the  $2p-1s$  transition) over those in the Wien tail of an equilibrium blackbody spectrum, and would therefore have been rapidly re-absorbed.

Understanding hydrogen recombination at the level required for sub-percent accuracy in CMB observables is both a challenging and ongoing activity. A major step forward was made in [35] where a number of approximations made in the original calculations

were improved upon. However, this improved calculation still misses a number of effects that are thought to influence the CMB power spectra by more than 1% for  $l > 1500$  and so there has been a flurry of recent activity in this area driven by the imminent launch of the Planck satellite. For a recent review of some of the issues involved, see [36].

### 2.3. Linear anisotropy generation: gravity

We shall mostly be concerned with linearised scalar (density) perturbations about spatially-flat models in general relativity. It is convenient to work in the conformal Newtonian gauge in which the spacetime metric is

$$ds^2 = a^2(\eta)[(1 + 2\psi)d\eta^2 - (1 - 2\phi)d\mathbf{x}^2], \quad (9)$$

where  $\eta$  is conformal time (related to proper time  $t$  by  $dt = a d\eta$ ),  $a$  is the scale factor in the background model and  $\mathbf{x}$  is comoving position. The physics of the CMB is particularly intuitive in this gauge. The two scalar potentials  $\phi$  and  $\psi$  represent the scalar perturbation to the metric, and play a similar role to the Newtonian gravitational potential. In the absence of anisotropic stress in matter and fields,  $\phi = \psi$ .

We parameterise a CMB photon by its energy  $\varepsilon/a$  as seen by an observer at rest in our coordinate system, where  $\varepsilon$  is the *comoving energy*, and the direction cosines  $\mathbf{e} = (e^1, e^2, e^3)$ , with  $\mathbf{e}^2 = 1$ , relative to an orthonormal triad of spatial vectors,  $a^{-1}(1 + \phi)\partial_i$ . The comoving energy is constant in the absence of metric perturbations. The photon four-momentum is then

$$p^\mu = a^{-2}\varepsilon[1 - \psi, (1 + \phi)\mathbf{e}]. \quad (10)$$

We write the photon distribution function,  $f(x^\mu, p^\mu)$ , as the sum of a background part  $\bar{f}(\varepsilon)$ , which is a Planck function with  $E/\bar{T}(\eta) = \varepsilon/(a\bar{T})$  and so has no explicit time dependence as  $a\bar{T}(\eta) = \text{const.}$ , and a linear perturbation. Denoting small changes in the temperature of the radiation for different directions by  $\bar{T}(\eta)\Theta(\mathbf{e})$ , the perturbation to the distribution function can be written as  $-\Theta(\mathbf{e})\varepsilon d\bar{f}/d\varepsilon$  so that

$$f(\eta, \mathbf{x}, \varepsilon, \mathbf{e}) = \bar{f}(\varepsilon)[1 - \Theta(\eta, \mathbf{x}, \mathbf{e})d\ln\bar{f}(\varepsilon)/d\ln\varepsilon]. \quad (11)$$

The quadrupole and higher multipoles of the fractional temperature fluctuation  $\Theta$  are gauge-invariant.

The distribution function is conserved along the photon path in phase space when there is no scattering. Parameterising the path with  $\eta$ , we have  $d\mathbf{x}/d\eta = (1 + \phi + \psi)\mathbf{e}$  from  $p^\mu = dx^\mu/d\lambda$  (with  $\lambda$  an affine parameter). The evolution of  $\varepsilon$  and  $\mathbf{e}$  follows from the geodesic equation; at linear order

$$d\varepsilon/d\eta = -\varepsilon d\psi/d\eta + \varepsilon(\dot{\phi} + \dot{\psi}), \quad (12)$$

$$d\mathbf{e}/d\eta = -(\nabla - \mathbf{e}\mathbf{e} \cdot \nabla)(\phi + \psi), \quad (13)$$

where overdots denote differentiation with respect to  $\eta$  and  $d\psi/d\eta = \dot{\psi} + \mathbf{e} \cdot \nabla\psi$  is the derivative of  $\psi$  along the photon path. The comoving energy thus evolves due to variation in the gravitational potentials experienced by the photon, and the direction

is deflected by the gradient of  $\phi + \psi$  perpendicular to  $\mathbf{e}$  (i.e. gravitational lensing). The derivative of the distribution function along the spacetime path *at fixed  $\varepsilon$  and  $\mathbf{e}$*  is sourced by the gravitational redshifting in Eq. (12), so that

$$\left. \frac{d\Theta(\eta, \mathbf{x}, \mathbf{e})}{d\eta} \right|_{\text{grav}} = \left( \frac{\partial}{\partial \eta} + \mathbf{e} \cdot \nabla \right) \Theta \Big|_{\text{grav}} = -\frac{d\psi}{d\eta} + \dot{\phi} + \dot{\psi}. \quad (14)$$

The gravitational lensing effect does not contribute at linear order since the zero-order distribution function  $\bar{f}$  is isotropic. If our observation event has coordinates  $(\eta_R, \mathbf{x}_R)$ , a photon would have last scattered around recombination at the event  $(\eta_*, \mathbf{x}_*)$ , where  $\eta_* = \eta_R - \chi_*$  and  $\mathbf{x}_* = \mathbf{x}_R - \mathbf{e}\chi_*$ . On integrating Eq. (14) between these events, the first term on the right produces a temperature perturbation given by the difference between  $\psi$  at last scattering and at reception. A photon suffers a net redshift if it climbs out of a deeper potential well than it is received in and this corresponds to a negative temperature fluctuation. The second term on the right of Eq. (14) gives the integrated Sachs-Wolfe contribution to  $\Theta$ ,

$$\Theta_{\text{ISW}} = \int_*^R (\dot{\phi} + \dot{\psi}) d\eta, \quad (15)$$

where the integral is taken along the line of sight. At linear order, the only contributions to this integral are from the evolution of the potentials around recombination, due to the duration of the matter-radiation transition (the early ISW effect), and the late-time ISW effect, when the potentials decay as dark energy becomes dynamically important. For the latter, in traversing a potential well that is getting shallower in time (i.e.  $\dot{\phi} + \dot{\psi} > 0$ ), photons receive a net blueshift and a positive contribution to  $\Theta$ .

## 2.4. Linear anisotropy generation: scattering

The dominant scattering mechanism to affect CMB anisotropies is classical Thomson scattering off non-relativistic, free electrons (with proper number density  $n_e$ ). The evolution of the temperature fluctuation due to scattering takes the form

$$\left. \frac{d\Theta}{d\eta} \right|_{\text{scattering}} = -an_e\sigma_T\Theta + \frac{3an_e\sigma_T}{16\pi} \int d\hat{\mathbf{m}} \Theta(\varepsilon, \hat{\mathbf{m}}) [1 + (\mathbf{e} \cdot \hat{\mathbf{m}})^2] + an_e\sigma_T\mathbf{e} \cdot \mathbf{v}_b, \quad (16)$$

where  $\sigma_T$  is the Thomson cross-section. The first term on the right describes scattering out of the beam; the second, scattering into the beam and involves the familiar  $1 + \cos^2 \theta$  dependence where  $\theta$  is the scattering angle; the final term is a Doppler effect that arises from the peculiar (bulk) velocity of the electrons,  $\mathbf{v}_b = d\mathbf{x}/d\eta$ . For the latter, scattering from a moving electron boosts the energy of a photon scattered in the direction that the electron is moving. Note that the effect of scattering vanishes for an isotropic distribution function and  $\mathbf{v}_b = 0$ . If we neglect the anisotropic nature of Thomson scattering, replacing  $1 + \cos^2 \theta$  by its angular average  $4/3$ , Eq. (16) reduces to

$$\left. \frac{d\Theta}{d\eta} \right|_{\text{scattering}} \approx -an_e\sigma_T(\Theta - \Theta_0 - \mathbf{e} \cdot \mathbf{v}_b), \quad (17)$$



where  $\Theta_0 = \int \Theta d\mathbf{e}/(4\pi)$  is the monopole of the temperature fluctuation (which equals  $\delta_\gamma/4$  with  $\delta_\gamma$  the photon energy density contrast). As expected, scattering tends to isotropise the photons in the baryon rest frame,  $\Theta \rightarrow \Theta_0 + \mathbf{e} \cdot \mathbf{v}_b$ .

Combining the gravitational and scattering contributions gives the Boltzmann equation for  $\Theta$ , which is most conveniently written as

$$\begin{aligned} \frac{d}{d\eta} [e^{-\tau}(\Theta + \psi)] &= -\dot{\tau}e^{-\tau} \left( \psi + \mathbf{e} \cdot \mathbf{v}_b + \frac{3}{16\pi} \int d\hat{\mathbf{m}} \Theta(\boldsymbol{\varepsilon}, \hat{\mathbf{m}}) [1 + (\mathbf{e} \cdot \hat{\mathbf{m}})^2] \right) \\ &+ e^{-\tau}(\dot{\phi} + \dot{\psi}), \end{aligned} \quad (18)$$

where  $\tau(\eta) \equiv \int_\eta^{\eta_R} an_e \sigma_T d\eta'$  is the optical depth to Thomson scattering. The quantity  $-\dot{\tau}e^{-\tau}$  is the (conformal) visibility function, introduced in Sec. 2.2.

A formal solution to Eq. (18) can be found by integrating along the line of sight from some early time, when  $\tau \rightarrow \infty$ , to the reception event  $R$  where  $\tau = 0$ :

$$[\Theta(\mathbf{e}) + \psi]_R = \int_0^R S d\eta, \quad (19)$$

with  $S$  the source term on the right-hand side of Eq. (18). The standard Boltzmann codes, CMBFAST [37] and CAMB [38] evaluate this integral directly and efficiently by expanding the source term in Fourier modes. For our purposes here, we gain useful insight into the physics of anisotropy formation by approximating last scattering as instantaneous, in which case the visibility function is a delta-function, and ignoring the effect of reionization and the anisotropic nature of Thomson scattering; Eq. (19) then approximates to

$$[\Theta(\mathbf{e}) + \psi]_R = \Theta_0|_* + \psi_* + \mathbf{e} \cdot \mathbf{v}_b|_* + \int_*^R (\dot{\phi} + \dot{\psi}) d\eta. \quad (20)$$

The various terms have a simple physical interpretation. The temperature received along  $\mathbf{e}$  is the isotropic temperature of the CMB at the last scattering event on the line of sight,  $\Theta_0|_*$ , corrected for the gravitational redshift due to the difference in the potential  $\psi_* - \psi_R$ , and the Doppler shift  $\mathbf{e} \cdot \mathbf{v}_b|_*$  resulting from scattering off moving electrons. Finally, there is the integrated Sachs-Wolfe contribution from evolution of the potentials along the line of sight.

### 2.4.1. Spatial-to-angular projection

The main contribution to the CMB temperature anisotropies comes from the projection of  $\Theta_0 + \psi$  at the time of last scattering onto the sphere of radius  $\chi_*$  centred on  $\mathbf{x}_R$ . For a general, statistically homogeneous and isotropic field  $f(\mathbf{x})$ , with a Fourier representation

$$f(\mathbf{x}) = \int \frac{d^3\mathbf{k}}{(2\pi)^{3/2}} f(\mathbf{k}) e^{i\mathbf{k} \cdot \mathbf{x}}, \quad (21)$$

the spherical multipoles of the projection of  $f$  on the sphere  $|\mathbf{x} - \mathbf{x}_R| = \chi_*$  are

$$f_{lm} = 4\pi i^l \int \frac{d^3\mathbf{k}}{(2\pi)^{3/2}} f(\mathbf{k}) j_l(k\chi_*) Y_{lm}^*(\hat{\mathbf{k}}) e^{i\mathbf{k}\cdot\mathbf{x}_R}. \quad (22)$$

Here,  $j_l(k\chi_*)$  are spherical Bessel functions. For large  $l$  they peak sharply around  $k\chi_* = l$  so that the multipoles  $f_{lm}$  receive their majority contribution from Fourier modes of wavenumber  $k \sim l/\chi_*$ . For any line of sight, such wavevectors aligned perpendicular to the line of sight give angular structure on the sky with characteristic period  $2\pi/(k\chi_*) \sim 2\pi/l$  matching that of  $Y_{lm}(\hat{\mathbf{n}})$ . The  $j_l(k\chi_*)$  have oscillatory tails for  $k\chi_* \gg l$  so that modes with  $k > l/\chi_*$  also contribute to the  $f_{lm}$ ; this corresponds to shorter wavelength Fourier modes not oriented perpendicular to the line of sight. Introducing the dimensionless power spectrum,  $\mathcal{P}_f(k)$ , of  $f(\mathbf{x})$ ,

$$\langle f(\mathbf{k}) f^*(\mathbf{k}') \rangle = \frac{2\pi^2}{k^3} \mathcal{P}_f(k) \delta(\mathbf{k} - \mathbf{k}'), \quad (23)$$

the angular power spectrum of the projection is

$$C_l^f = 4\pi \int \mathcal{P}_f(k) j_l^2(k\chi_*) d \ln k. \quad (24)$$

The contribution to  $C_l^T$  from  $\Theta_0 + \psi$  at last scattering takes this form with  $f = \Theta_0 + \psi$ .

The arguments for the projection of a field that is locally a dipole, like  $\mathbf{e} \cdot \mathbf{v}_b$ , are a little different. For scalar perturbations, the Fourier components of  $\mathbf{v}_b$  take the form  $i\hat{\mathbf{k}}v_b(\mathbf{k})$  and so the projection of  $\mathbf{e} \cdot \mathbf{v}_b$  has multipoles

$$(\mathbf{e} \cdot \mathbf{v}_b)_{lm} = -4\pi i^l \int \frac{d^3\mathbf{k}}{(2\pi)^{3/2}} v_b(\mathbf{k}) j_l'(k\chi_*) Y_{lm}^*(\hat{\mathbf{k}}) e^{i\mathbf{k}\cdot\mathbf{x}_R}. \quad (25)$$

Here,  $j_l'(k\chi_*)$  is the derivative of  $j_l(k\chi_*)$  with respect to its argument. It does not have the same prominent peak as  $j_l(k\chi_*)$ , rather having positive and negative wings either side of  $k\chi_* = l$ . The projection from  $k$  to  $l$  is therefore much less sharp for terms that are locally a dipole compared to monopole terms. Physically, this arises because there is no contribution to the projection of  $\mathbf{e} \cdot \mathbf{v}_b$  from Fourier modes with their wavevector perpendicular to the line of sight.

## 2.5. Acoustic physics

The photon isotropic temperature perturbation  $\Theta_0 = \delta_\gamma/4$  and baryon velocity  $\mathbf{v}_b$  depend on the acoustic physics of the pre-recombination plasma. Before recombination, the comoving mean-free path of CMB photons is

$$l_p = (an_e \sigma_T)^{-1} = -\dot{\tau}^{-1} \approx 4.9 \times 10^4 (\Omega_b h^2)^{-1} (1+z)^{-2} \text{ Mpc}. \quad (26)$$

On scales larger than this, Thomson scattering keeps the photons isotropic in the baryon rest frame and the photon-baryon system can be modelled as a tightly-coupled fluid

characterised by a single peculiar velocity  $\mathbf{v}_b$ . The Euler equation for this system, in the Newtonian gauge, is

$$\dot{\mathbf{v}}_b + \frac{R}{1+R} \mathcal{H} \mathbf{v}_b + \frac{1}{4(1+R)} \nabla \delta_\gamma + \nabla \psi = 0, \quad (27)$$

where  $R \equiv \bar{\rho}_b/(\bar{\rho}_\gamma + \bar{p}_\gamma) = 3\bar{\rho}_b/(4\bar{\rho}_\gamma) \propto a$  and  $\bar{\rho}_i$  and  $\bar{p}_i$  are the unperturbed energy density and pressure of species  $i$ . The drag term, involving the conformal Hubble parameter  $\mathcal{H} \equiv \dot{a}/a$ , arises since the peculiar velocity of non-relativistic massive particles (the baryons) decays as  $1/a$  in an expanding universe. The  $\nabla \delta_\gamma$  term comes from the gradient of the photon pressure. This acts on the full inertia of the photon-baryon system and so its effect reduces for increasing  $R$ . The final term describes (universal) gravitational infall in the potential gradient  $\nabla \psi$ . The energy density of the photons is not changed by scattering off cold electrons and so  $\delta_\gamma$  evolves as for a non-interacting photon gas:

$$\dot{\delta}_\gamma + \frac{4}{3} \nabla \cdot \mathbf{v}_b - 4\dot{\phi} = 0. \quad (28)$$

The second and third terms in this equation are the usual  $\bar{\rho} + \bar{p}$  times volume expansion rate, where the perturbed expansion rate receives contributions from  $\nabla \cdot \mathbf{v}_b$  and the perturbation  $-3\dot{\phi} d^3\mathbf{x}$  to the volume element (see Eq. (9)).

Combining Eqs (27) and (28) gives the equation of a damped, harmonic oscillator driven by gravity [39]:

$$\ddot{\delta}_\gamma + \frac{\mathcal{H}R}{1+R} \dot{\delta}_\gamma - \frac{1}{3(1+R)} \nabla^2 \delta_\gamma = 4\ddot{\phi} + \frac{4\mathcal{H}R}{1+R} \dot{\phi} + \frac{4}{3} \nabla^2 \psi. \quad (29)$$

First, consider the solutions to the homogeneous equation, ignoring the effects of gravity. On sub-Hubble scales,  $k \gg \mathcal{H}$ , the WKB approximation can be used to show that

$$\delta_\gamma = (1+R)^{-1/4} \cos kr_s \quad \text{and} \quad \delta_\gamma = (1+R)^{-1/4} \sin kr_s, \quad (30)$$

are independent solutions, where the *sound horizon*  $r_s \equiv \int_0^\eta d\eta' / \sqrt{3(1+R)}$ . These are acoustic oscillations at instantaneous frequency  $k/\sqrt{3(1+R)}$ , where  $1/\sqrt{3(1+R)}$  is the sound speed of the photon-baryon system, with a slow decay in amplitude. We shall show shortly that for *adiabatic initial conditions*, as expected in single-field models of inflation, the system oscillates essentially in the cosine mode. All Fourier modes of a given  $k$ , irrespective of the direction of their wavevector, reach extrema of their acoustic oscillations at the same time. This *phase coherence* is an inevitable consequence of the dominance of a single “growing mode” in the primordial perturbation at the end of inflation, and is not present in models that continually source perturbations such as those with topological defects [40]. Phase coherence implies a series of acoustic peaks in the CMB angular power spectrum (see Fig. 2) at multipoles  $l$  such that  $l/\chi_*$  corresponds to the wavenumber of modes that have reached extrema at  $\eta_*$ . For adiabatic initial conditions, the acoustic peaks are located approximately at  $l = n\pi\chi_*/r_s(\eta_*)$ .

### 2.5.1. Initial conditions and gravitational driving

We can get the initial conditions for the oscillator deep in the radiation era by considering the self-gravitating perturbations of a radiation fluid. Such a treatment makes a number of assumptions. First, neutrinos are treated as a fluid but, after decoupling, they actually free-stream and so do not cluster appreciably on sub-Hubble scales. Moreover, free-streaming generates anisotropic stress  $\sim \bar{\rho}_\nu (k\eta)^2 \phi$  in the neutrinos which produces a time-independent 14% offset between (the constant)  $\phi$  and  $\psi$  on large scales. Second, we are assuming that the perturbations in the baryonic matter and CDM have a negligible effect on the gravitational potentials. This is appropriate for adiabatic initial conditions deep in the radiation era, where all species are initially distributed homogeneously on large scales on the same spacetime hypersurfaces, i.e. the density perturbations of all species vanish on hypersurfaces over which the total density perturbation vanishes. In any other gauge,  $\bar{\rho}_i \delta_i / \dot{\bar{\rho}}_i$  is equal for all species and there are therefore no relative perturbations in the number density of particles. For adiabatic initial conditions, the total energy density contrast in the radiation era is dominated by the radiation perturbations. This should be compared to isocurvature initial conditions, where, for example, the CDM density contrast is initially much larger than the radiation contrast in such a way as to give no net curvature perturbation.

In a radiation fluid,  $\mathcal{H} = 1/\eta$  and the trace of the  $ij$  Einstein equation (see, for example, [41]) gives

$$\ddot{\phi} + \frac{3}{\eta} \dot{\phi} - \frac{1}{\eta^2} \phi = \frac{1}{2\eta^2} \delta_r, \quad (31)$$

where the subscript  $r$  denotes radiation (photons plus neutrinos). The 00 Einstein equation is

$$\nabla^2 \phi = \frac{3}{\eta^2} (\eta \dot{\phi} + \phi) + \frac{3}{2\eta^2} \delta_r, \quad (32)$$

so the potential evolves as

$$\ddot{\phi} + \frac{4}{\eta} \dot{\phi} - \frac{1}{3} \nabla^2 \phi = 0, \quad (33)$$

with regular (growing-mode) solution  $\phi \propto j_1(k\eta/\sqrt{3})/(k\eta)$ . This is constant outside the sound horizon,  $k\eta \ll \sqrt{3}$ , but undergoes decaying oscillations on small scales with asymptotic behaviour<sup>2</sup>  $\phi \propto -\sqrt{3} \cos(k\eta/\sqrt{3})/(k\eta)^2$ . Solving for  $\delta_r$  from Eq. (32) gives a solution with  $\delta_r = -2\phi(0)$  on large scales (i.e.  $\delta_r$  is constant) and constant amplitude oscillations,  $\delta_r = -6 \cos(k\eta/\sqrt{3})\phi(0)$ , well inside the sound horizon. As advertised above, adiabatic initial conditions excite the cosine mode of the oscillator. Note also that the radiation starts off over-dense in potential wells.

If we now return to Eq. (29), we can make two important observations that affect the height of the acoustic peaks in the CMB power spectrum. First, for modes that enter the sound horizon between matter-radiation equality and recombination, the oscillations occur in potentials that approximately equal the primordial value  $\phi(0)$ . More carefully,

---

<sup>2</sup> The presence of the CDM, which does not undergo acoustic oscillations, leads to a  $k$ -dependent offset,  $\sim k^{-2} \ln k$ , in the oscillation as the matter-radiation transition is approached.

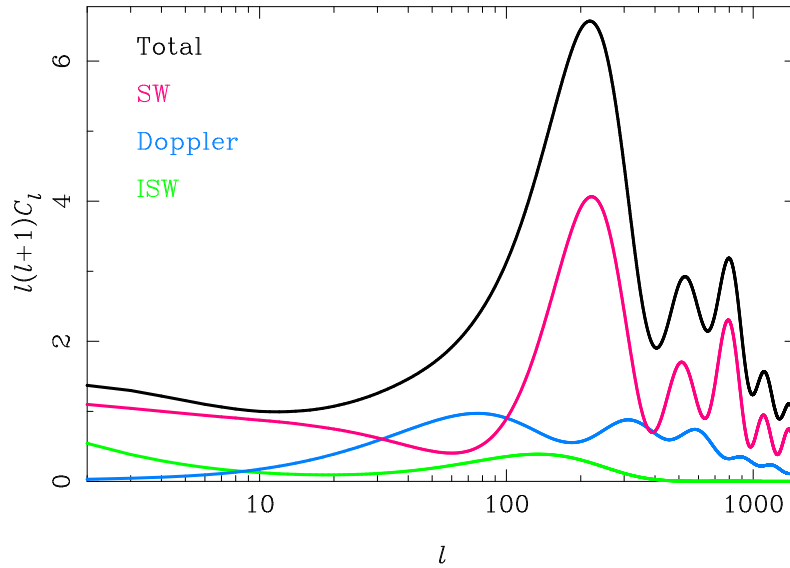


**FIGURE 3.** Contribution of the various terms in Eq. (20) to the temperature-anisotropy power spectrum from adiabatic initial conditions:  $\delta_\gamma/4 + \psi$  (denoted SW for Sachs-Wolfe [42]; magenta); Doppler effect from  $v_b$  (blue); and the integrated Sachs-Wolfe effect (ISW; green) coming from evolution of the potential along the line of sight. The units of the spectrum are arbitrary.

the potential decays by 10% through the matter-radiation transition on large scales – although this is not complete at recombination – and, by Eq. (28),  $\delta_\gamma$  is enhanced by 20%. The potential shifts the midpoint of the oscillation to  $\delta_\gamma \approx -4(1+R)\psi$  which corresponds to the over-density needed for photon pressure to balance gravitational infall. Since baryons contribute to the inertia but not the pressure, they enhance  $\delta_\gamma$  at the midpoint. The source term for the temperature anisotropy,  $\Theta_0 + \psi = \delta_\gamma/4 + \psi$ , therefore oscillates about  $-R\psi$  with an amplitude of  $3\phi(0)/10$  (ignoring non-zero  $R$  in the amplitude). The dependence of the midpoint on the baryon density makes the relative heights of the first few acoustic peaks sensitive to the baryon density. The second observation is that for modes shorter than the sound horizon at matter-radiation equality, the decay of the potential during the oscillations in the radiation renders the driving term on the right of Eq. (29) negligible during the matter era. However, our treatment of the radiation fluid above shows that the driving term acts resonantly around the time of sound-horizon crossing in the radiation era and enhances the amplitude of the acoustic oscillation of  $\delta_\gamma/4$  towards the asymptotic value  $3\phi(0)/2$ , five times the value on large scales. Increasing the matter density limits the scales for which resonant driving is effective to smaller scales. In practice, diffusion damping (see Sec. 2.7) exponentially damps the amplitude of the oscillations on small scales and the asymptotic amplitude is not attainable.

## 2.6. $C_l^T$ for adiabatic initial conditions

The contributions of the various terms in Eq. (20) to the temperature anisotropy power spectrum for adiabatic initial conditions are shown in Fig. 3. The main contribution is from  $\Theta_0 + \psi$ . The plateau on large scales comes from modes that have not had time to oscillate by recombination; for such modes,  $\Theta_0 + \psi \approx 3\phi(0)/10 = \phi/3$ . It is convenient to express the initial value of the potential in terms of the comoving-gauge curvature perturbation,

$$\mathcal{R} \equiv -\phi - \frac{\mathcal{H}(\dot{\phi} + \mathcal{H}\psi)}{4\pi G a^2(\bar{\rho} + \bar{p})}, \quad (34)$$

which is conserved on super-Hubble scales for adiabatic perturbations independent of the equation of state relating the total pressure  $\bar{p}$  and energy density  $\bar{\rho}$ . During radiation domination,  $\mathcal{R} = -3\phi(0)/2$  ignoring neutrino anisotropic stress, and so on large scales  $\Theta_0 + \psi \approx -\mathcal{R}/5$ . This directly relates  $C_l^T$  to the primordial power spectrum  $\mathcal{P}_{\mathcal{R}}(k)$  (which is calculable given a model of inflation) on large scales. In particular, a nearly scale-invariant  $\mathcal{P}_{\mathcal{R}}(k)$  projects to give  $l(l+1)C_l \approx \text{const}$ . The prominent acoustic peaks in Fig. 3 reflect the acoustic oscillations of the photon-baryon system. The first peak corresponds to modes that have just reached the first maximum of their oscillation by last scattering. The resonant-driving arguments given earlier suggest that the acoustic peaks should grow in amplitude with increasing  $l$ . In practice, an exponential decline in power is seen because of diffusion damping.

The late-time ISW effect adds power incoherently to the contribution from recombination since the former is sourced at late times. However, the early-ISW effect, which peaks close to the first acoustic peak, adds power coherently [39]. It enhances the first peak considerably since  $\dot{\phi} + \dot{\psi}$  has the same sign, i.e. positive in potential wells, as  $\Theta_0 + \psi$ . It is less important for the higher peaks since the potential at last scattering for these is suppressed by the acoustic oscillations during radiation domination.

The baryon peculiar velocity oscillates  $\pi/2$  out of phase with  $\delta_\gamma$  by Eq. (28), and so the Doppler term tends to fill in the troughs of the angular power spectrum. The oscillatory structure would be destroyed completely were it not for two effects: the geometric effect noted for the projection of dipole-like fields in Sec. 2.4, and the effect of baryons. The latter shift the midpoint of the oscillations in  $\Theta_0 + \psi$  from zero, so its zeroes do not coincide with the extrema of the peculiar velocity. Furthermore, baryons reduce the amplitude of the oscillations in  $\mathbf{v}_b$  by a factor of  $\sqrt{1+R}$ .

## 2.7. Complications to the simple picture

### 2.7.1. Photon diffusion

On small scales, the CMB anisotropies are exponentially damped due to photon diffusion. Before recombination, fluctuations with wavelengths comparable to or smaller than the mean-free path of photons to Thomson scattering are damped out, as photons can diffuse out of over-dense regions into neighbouring under-densities. How far will a photon have diffused by last scattering? To answer this, consider the comoving mean-

free path of the photons,  $l_p$ , which is related to the Thomson cross section and the number density of free electrons via

$$l_p = \frac{1}{an_e\sigma_T}. \quad (35)$$

In some interval of conformal time,  $d\eta$ , a photon undergoes  $d\eta/l_p$  scatterings and random walks through a mean-squared distance  $l_p^2 d\eta/l_p = l_p d\eta$ . The total mean-squared distance that a photon will have moved by such a random walk by the time  $\eta_*$  is therefore

$$\int_0^{\eta_*} \frac{d\eta'}{an_e\sigma_T} \sim \frac{1}{k_D^2}, \quad (36)$$

which defines a damping scale  $k_D^{-1}$ . The photon density and velocity perturbations at wavenumber  $k$  are damped exponentially by photon diffusion, going like  $e^{-k^2/k_D^2}$ ; this produces a similar damping in the angular power spectrum  $C_l$  (see Fig. 3). Evaluating  $k_D$  around recombination gives a comoving damping scale  $\sim 30$  Mpc.

### 2.7.2. Reionization

Once structure formation had proceeded to produce the first sources of ionizing radiation, neutral hydrogen and helium began to reionize. The resulting free electron density could then re-scatter CMB photons, and this affected the observed CMB in several ways. The only significant effect for the temperature anisotropies in linear theory is a uniform screening by  $e^{-\tau_{\text{re}}}$ , where  $\tau_{\text{re}}$  is the optical depth through reionization, on scales  $l > 10$ . Anisotropies on such scales are generated from perturbations that are sub-Hubble at the time of reionization. For these modes, the radiation is already significantly anisotropic at reionization since the perturbations vary significantly over the scattering electron's own last-scattering surface. The net effect of in-scattering from different lines of sight thus averages to zero, leaving a suppression by  $e^{-\tau_{\text{re}}}$  due to scattering out of the line of sight. In the power spectrum, this becomes  $e^{-2\tau_{\text{re}}}$ . However, Fourier modes that are still super-Hubble at reionization produce negligible *anisotropy* by the time of reionization since the perturbations over the scattering electron's own last scattering surface are almost uniform. Scattering isotropic radiation has no effect, and so reionization does not alter the temperature anisotropies from recombination for  $l < 10$ . Scattering around reionization also generates new large-angle polarization – see Sec. 3.3 – and, at second-order, small-scale temperature anisotropies; see Sec. 6.2.

Note that screening at reionization makes the determination of the amplitude and shape of the primordial power spectrum from temperature data alone rather degenerate with  $\tau_{\text{re}}$ .

### 2.7.3. Gravitational waves

Tensor modes, describing gravitational waves, represent the transverse trace-free perturbations to the spatial metric:

$$ds^2 = a^2(\eta)[d\eta^2 - (\delta_{ij} + h_{ij})dx^i dx^j], \quad (37)$$

with  $h_i^i = 0$  and  $\partial_i h_j^i = 0$ . A convenient parameterisation of the photon four-momentum in this case is

$$p^\mu = \frac{\varepsilon}{a^2} \left[ 1, e^i - \frac{1}{2} h_j^i e^j \right], \quad (38)$$

where, as for scalar perturbations,  $e^2 = 1$  and  $\varepsilon$  is  $a$  times the energy of the photon as seen by an observer at constant  $\mathbf{x}$ . The components of  $\mathbf{e}$  are the direction cosines of the photon direction for this observer on an orthonormal spatial triad of vectors  $a^{-1}(\partial_i - h_i^j \partial_j/2)$ , and are constant in the unperturbed universe. The evolution of the comoving energy,  $\varepsilon$ , follows from the geodesic equation:

$$\frac{1}{\varepsilon} \frac{d\varepsilon}{d\eta} + \frac{1}{2} \dot{h}_{ij} e^i e^j = 0, \quad (39)$$

and so the Boltzmann equation for the fractional temperature anisotropies is

$$\begin{aligned} \frac{\partial \Theta}{\partial \eta} + \mathbf{e} \cdot \nabla \Theta &= -an_e \sigma_T \Theta + \frac{3an_e \sigma_T}{16\pi} \int d\hat{\mathbf{m}} \Theta(\varepsilon, \hat{\mathbf{m}}) [1 + (\mathbf{e} \cdot \hat{\mathbf{m}})^2] \\ &\quad - \frac{1}{2} \dot{h}_{ij} e^i e^j. \end{aligned} \quad (40)$$

All perturbed scalar and vector quantities vanish for tensor perturbations so  $\Theta(\mathbf{e})$  has only  $l \geq 2$  moments. Neglecting the anisotropic nature of Thomson scattering, or, equivalently, the temperature quadrupole at last scattering, the solution of Eq. (40) is an integral along the unperturbed line of sight:

$$[\Theta(\mathbf{e})]_R = -\frac{1}{2} \int_*^R e^{-\tau} \dot{h}_{ij} e^i e^j d\eta. \quad (41)$$

The physics behind this solution is as follows. The time derivative  $\dot{h}_{ij}$  is the shear induced by the gravitational waves. This quadrupole perturbation to the expansion rate produces an anisotropic redshifting of the CMB photons and an associated temperature anisotropy.

The shear source term for the tensor anisotropies is locally a quadrupole since  $\dot{h}_{ij}$  is trace-free. Projecting this contribution at a given time onto angular multipoles on the sky is a little more involved than for scalar perturbations [43]. We start by decomposing  $\dot{h}_{ij}$  into circularly-polarized Fourier modes,

$$h_{ij} = \sum_{\pm} \int \frac{d^3 \mathbf{k}}{(2\pi)^{3/2}} h_{ij}^{(\pm 2)}(\mathbf{k}) e^{i\mathbf{k} \cdot \mathbf{x}}, \quad h_{ij}^{(\pm 2)}(\mathbf{k}) = \frac{1}{\sqrt{2}} m_{ij}^{(\pm 2)}(\mathbf{k}) h^{(\pm 2)}(\mathbf{k}). \quad (42)$$



Here, the basis tensors  $m_{ij}^{(\pm 2)}(\mathbf{k})$  are complex, symmetric trace-free and orthogonal to  $\mathbf{k}$ , and  $h^{(\pm 2)}(\mathbf{k})$  are scalar Fourier amplitudes. For  $\mathbf{k}$  along the  $z$ -axis, we choose  $m_{ij}^{(\pm 2)} = (\hat{\mathbf{x}} \pm i\hat{\mathbf{y}})_i (\hat{\mathbf{x}} \pm i\hat{\mathbf{y}})_j / 2$ . For such Fourier modes the shear source is

$$\dot{h}_{ij}^{(\pm 2)}(k\hat{\mathbf{z}})e^i e^j \propto \frac{1}{2\sqrt{2}} [(\hat{\mathbf{x}} \pm i\hat{\mathbf{y}}) \cdot \mathbf{e}]^2 = \frac{1}{2\sqrt{2}} \sin^2 \theta e^{\pm 2i\phi} = \sqrt{\frac{4\pi}{15}} Y_{2\pm 2}(\mathbf{e}). \quad (43)$$

The projection of this at comoving distance  $\chi$  is

$$\begin{aligned} \sqrt{\frac{4\pi}{15}} Y_{2\pm 2}(\mathbf{e}) e^{-ik\chi \cos \theta} &= \frac{4\pi}{\sqrt{15}} \sum_L (-i)^L \sqrt{2L+1} j_L(k\chi) Y_{2\pm 2}(\mathbf{e}) Y_{L0}(\mathbf{e}) \\ &= \sqrt{\frac{4\pi}{3}} \sum_L \left[ (-i)^L (2L+1) j_L(k\chi) \right. \\ &\quad \left. \times \sum_l \sqrt{2l+1} \begin{pmatrix} 2 & L & l \\ \mp 2 & 0 & \pm 2 \end{pmatrix} \begin{pmatrix} 2 & L & l \\ 0 & 0 & 0 \end{pmatrix} Y_{l\pm 2}(\mathbf{e}) \right], \quad (44) \end{aligned}$$

where we have used the Rayleigh plane-wave expansion. The  $3j$  symbols arise from coupling the angular dependence of the source to that of the plane wave. Since they force  $L$  and  $l$  to have the same parity, the  $l$ th multipoles of the projection involve the  $l$  and  $l \pm 2$  multipoles of the plane wave. We can simplify further by writing out the  $3j$  symbols explicitly and using the recursion relations for Bessel functions to express  $j_{l\pm 2}$  in terms of  $j_l$ . The final result is remarkably compact:

$$\dot{h}_{ij}^{(\pm 2)}(k\hat{\mathbf{z}})e^i e^j e^{-ik\chi \cos \theta} = -\sqrt{\frac{\pi}{2}} \dot{h}^{(\pm 2)}(k\hat{\mathbf{z}}) \sum_l (-i)^l \sqrt{2l+1} \sqrt{\frac{(l+2)!}{(l-2)!}} \frac{j_l(k\chi)}{(k\chi)^2} Y_{l\pm 2}(\mathbf{e}). \quad (45)$$

The spatial-to-angular projection is now controlled by  $j_l(k\chi)/(k\chi)^2$ . As for scalar perturbations, this is concentrated on multipoles  $l \sim k\chi$ . The result for general  $\mathbf{k}$  can be obtained by a rotation  $\hat{D}(\phi_{\mathbf{k}}, \theta_{\mathbf{k}}, 0)$ , where  $\theta_{\mathbf{k}}$  and  $\phi_{\mathbf{k}}$  are the polar and azimuthal angles of  $\hat{\mathbf{k}}$  and the third Euler angle can be taken to be zero. Pre-empting a little the discussion in Sec. 3, we can relate the rotation matrices to spin-weighted spherical harmonics,  $D_{m\pm 2}^l(\phi_{\mathbf{k}}, \theta_{\mathbf{k}}, 0) = \sqrt{4\pi/(2l+1)} {}_{\mp 2} Y_{lm}^*(\hat{\mathbf{k}})$ , so that

$$\dot{h}_{ij}^{(\pm 2)}(\mathbf{k})e^i e^j e^{-i\chi \mathbf{k} \cdot \mathbf{e}} = -\sqrt{2\pi^2} \dot{h}^{(\pm 2)}(\mathbf{k}) \sum_{lm} (-i)^l \sqrt{\frac{(l+2)!}{(l-2)!}} \frac{j_l(k\chi)}{(k\chi)^2} {}_{\mp 2} Y_{lm}^*(\hat{\mathbf{k}}) Y_{lm}(\mathbf{e}). \quad (46)$$

This generalises the scalar result for which the multipoles were given in Eq. (22).

Figure 4 compares the power spectra due to gravitational waves with those from scalar perturbations. The former is shown at the maximum amplitude allowed by current data. Note that the spectra from gravitational waves fall sharply on scales that are sub-Hubble at recombination ( $l > 60$ ) since the amplitude of gravitational waves decays away as  $1/a$  inside the Hubble radius. This limits the power of temperature anisotropies

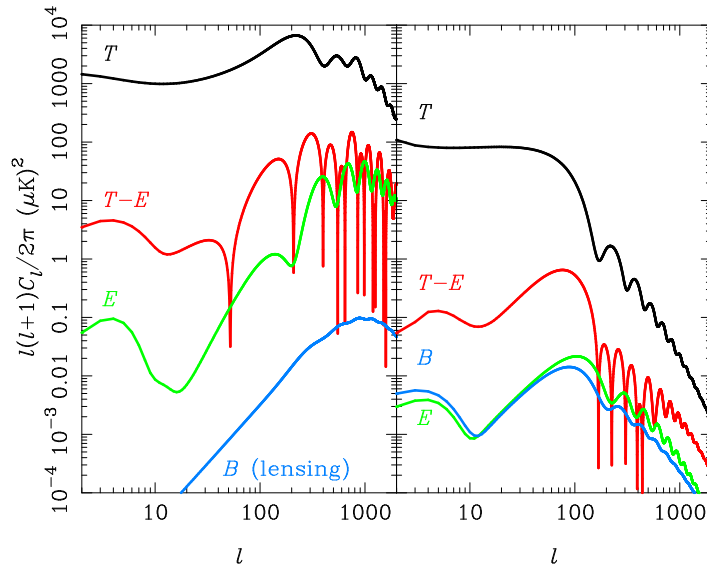


**FIGURE 4.** Temperature (black),  $E$ -mode (green),  $B$ -mode (blue) and  $T$ - $E$  cross-correlation (red) CMB power spectra from scalar perturbations (left) and tensor perturbations (gravitational waves; right). The amplitude of the tensor perturbations is shown at the maximum amplitude allowed by current data ( $r = 0.22$  [44]). The  $B$ -mode spectrum induced by weak gravitational lensing is also shown in the left-hand panel (blue; see Sec. 6.1.2).

to constrain gravitational waves since the sampling variance of the dominant scalar perturbations is large at low  $l$ . Fortunately, CMB polarization provides an alternative route to detecting the effect of gravitational waves on the CMB which is not limited by cosmic variance [45, 46]; see Sec. 3.

#### 2.7.4. Isocurvature modes

Adiabatic fluctuations are a generic prediction of single-field inflation models. However, multiple scalar fields typically arise in models inspired by high-energy physics, such as the axion model [47], curvaton [48] and multi-field inflation [49, 50]. In such models, if the fields decay asymmetrically and the decay products are unable to reach chemical equilibrium with each other, an isocurvature contribution to the primordial perturbation will result. The simplest, and best-motivated, possibility is an isocurvature mode where initially the dominant fractional over-density is in the CDM, with a compensating (very small) fractional fluctuation in the radiation and baryons [51]. The amplitude of the CDM isocurvature mode is quantified by the gauge-invariant quantity  $\mathcal{S} \equiv \delta_c - 3\delta_\gamma/4$ , where  $\delta_c$  is the CDM fractional over-density. Generally,  $\mathcal{S}$  can be correlated with the curvature perturbation  $\mathcal{R}$ , for example in the curvaton and multi-field models.

In the CDM mode, the photons are initially unperturbed, as is the geometry:  $\delta_\gamma(0) = 0 = \phi(0)$  and  $\mathbf{v}_b = 0$ . The different equations of state of the CDM and radiation lead to the generation of a curvature perturbation. On large scales,  $\mathcal{R}$  grows like  $a$  in radiation

domination and is constant in matter domination with an asymptotic value  $\approx \mathcal{S}/3$ . The gravitational potential follows suit and, for super-Hubble modes at last scattering,  $\phi_* = -3\mathcal{R}_*/5 = -\mathcal{S}/5$ . On large scales  $\delta_\gamma/4 = \phi$  is preserved, so that the source term for the temperature anisotropies on large scales is  $\Theta_0 + \psi \approx -2\mathcal{S}/5$ . For a general mix of isocurvature and adiabatic perturbations, the large-angle temperature anisotropies are related to the primordial perturbations by  $\Delta T/T \sim -\mathcal{R}/5 - 2\mathcal{S}/5$ .

The evolution of the potential for isocurvature modes makes the driving term in Eq. (29) mimic the sine solution of the homogeneous equation, and so  $\delta_\gamma$  oscillates as  $\sin kr_s$  inside the sound horizon. This  $\pi/2$  phase difference compared to adiabatic initial conditions shifts the acoustic peaks to multipoles  $l = (n + 1/2)\pi\chi_*/r_s(\eta_*)$ . The different peak positions for isocurvature initial conditions allow the CMB to constrain their relative contribution to the total fluctuations. The constraints on isocurvature modes depend strongly on the assumptions made about the shape of the primordial power spectrum for  $\mathcal{S}$  and any correlations with  $\mathcal{R}$ . For uncorrelated, axion-type models with scale-free CDM isocurvature fluctuations, the ratio of the primordial spectra for  $\mathcal{S}$  to  $\mathcal{R} < 0.2$  from CMB data alone [44]. Recent constraints in more general models can be found in [52].

### 3. INTRODUCTION TO CMB POLARIZATION

As the universe recombines, the mean-free path to Thomson scattering grows and temperature anisotropies start to develop. Subsequent scattering of the CMB quadrupole generates partial linear polarization in the CMB [5]. The signal is small, with r.m.s.  $\sim 5 \mu\text{K}$ , but contains complementary information to the temperature anisotropies and is therefore being actively pursued by observers.

#### 3.1. Polarization observables

Polarized specific brightness is most conveniently described in terms of Stokes parameters  $I(\hat{\mathbf{n}}; \nu)$ ,  $Q(\hat{\mathbf{n}}; \nu)$ ,  $U(\hat{\mathbf{n}}; \nu)$  and  $V(\hat{\mathbf{n}}; \nu)$ . The  $I$  parameter is the total intensity,  $Q$  measures the difference in brightness between two orthogonal linear polarizations, and  $V$  measures the circular polarization. The  $U$  parameter, like  $Q$ , measures linear polarization and is defined as the difference in brightness between two linear polarizations at  $45^\circ$  to those used to define  $Q$ . Thomson scattering of the CMB does not generate circular polarization so we expect the primordial  $V = 0$ . The Stokes parameters  $Q$  and  $U$  are functions of frequency as well as direction. In linear theory, their frequency dependence follows that of the temperature anisotropies; dividing by the derivative of the CMB blackbody (i.e. Planck) brightness with respect to (log) temperature allows us to express the Stokes parameters as frequency-independent fractional *thermodynamic equivalent temperatures*. We shall denote the equivalent temperatures by  $Q(\hat{\mathbf{n}})$  and  $U(\hat{\mathbf{n}})$ .

The linear Stokes parameters depend on the choice of basis. For a line of sight  $\hat{\mathbf{n}}$ , we define the Stokes parameters on a local  $x$ - $y$  basis defined by  $-\hat{\theta}, \hat{\phi}$  of the spherical-polar basis at  $\hat{\mathbf{n}}$ . Note that  $-\hat{\theta}, \hat{\phi}$  and  $-\hat{\mathbf{n}} = \mathbf{e}$  – the radiation propagation direction – form a right-handed basis. The reader is cautioned that this convention differs from some

of the CMB literature, most notably [10]. Under the right-handed rotation about the propagation direction,  $\hat{\theta} \pm i\hat{\phi} \rightarrow e^{\pm i\psi}(\hat{\theta} \pm i\hat{\phi})$ , the complex polarization

$$Q \pm iU \rightarrow e^{\mp 2i\psi}(Q \pm iU), \quad (47)$$

and so  $Q \pm iU$  is said to be spin  $\mp 2$ . The complex polarization can be expanded in terms of a real scalar field  $\sum_{lm} E_{lm} Y_{lm}(\hat{\mathbf{n}})$  and a real pseudo-scalar field  $\sum_{lm} B_{lm} Y_{lm}(\hat{\mathbf{n}})$ , where the summations are over  $l \geq 2$ , as [10]

$$(Q \pm iU)(\hat{\mathbf{n}}) = \sum_{lm} (E_{lm} \mp iB_{lm})_{\mp 2} Y_{lm}(\hat{\mathbf{n}}). \quad (48)$$

Here, the  ${}_{\mp 2}Y_{lm}(\hat{\mathbf{n}})$  are spin- $\mp 2$  spherical harmonics [53]. Spin- $s$  spherical harmonics are defined by

$${}_s Y_{lm} = \sqrt{\frac{(l-|s|)!}{(l+|s|)!}} \bar{\partial}^s Y_{lm}, \quad (49)$$

where  $\bar{\partial}^{-|s|} \equiv (-1)^s \bar{\partial}^{|s|}$ . The spin-raising and lowering operators,  $\bar{\partial}$  and  $\bar{\partial}^\dagger$  have action

$$\bar{\partial}_s \eta = -\sin^s \theta (\partial_\theta + i \operatorname{cosec} \theta \partial_\phi) (\sin^{-s} \theta {}_s \eta) \quad (50)$$

$$\bar{\partial}_s^\dagger \eta = -\sin^{-s} \theta (\partial_\theta - i \operatorname{cosec} \theta \partial_\phi) (\sin^s \theta {}_s \eta) \quad (51)$$

when acting on a spin- $s$  quantity  ${}_s \eta$ . They raise and lower the spin by one unit respectively.

The decomposition of the polarization into  $E$  and  $B$  modes is analogous to writing a vector on the 2-sphere,  $V_a$ , as the sum of a gradient part,  $\nabla_a V_E$ , and a divergence-free part, which can always be written as  $\varepsilon_a{}^b \nabla_b V_B$  where  $\varepsilon_{ab}$  is the alternating tensor. The components of  $V_a$  on the null basis  $\mathbf{m}_\pm \equiv (\hat{\theta} \pm i\hat{\phi})/\sqrt{2}$  are then

$$\begin{aligned} V_+ &= \mathbf{V} \cdot \mathbf{m}_+ = \frac{1}{\sqrt{2}} (\partial_\theta + i \operatorname{cosec} \theta) V_E - \frac{i}{\sqrt{2}} (\partial_\theta + i \operatorname{cosec} \theta) V_B = -\frac{1}{\sqrt{2}} \bar{\partial} (V_E - iV_B), \\ V_- &= \mathbf{V} \cdot \mathbf{m}_- = \frac{1}{\sqrt{2}} (\partial_\theta - i \operatorname{cosec} \theta) V_E + \frac{i}{\sqrt{2}} (\partial_\theta - i \operatorname{cosec} \theta) V_B = -\frac{1}{\sqrt{2}} \bar{\partial}^\dagger (V_E + iV_B) \end{aligned} \quad (52)$$

We see that the spin-1  $V_+$  is written as the action of the spin-raising operator on the potential  $-V_E + iV_B$  whose real and imaginary parts are the (real)  $E$  and  $B$  potentials for  $\mathbf{V}$ . Things work similarly for polarization since  $Q \pm iU$  are the null components of a symmetric, trace-free tensor  $\mathcal{P}_{ab}$  [54].

To gain further intuition for  $E$  modes and  $B$  modes, consider the case where the potentials  $\sum_{lm} E_{lm} Y_{lm}(\hat{\mathbf{n}})$  and  $\sum_{lm} B_{lm} Y_{lm}(\hat{\mathbf{n}})$  behave locally like a plane wave across a small patch of the sky (that can accurately be treated as flat). The  $E$  and  $B$  contributions to the polarization are depicted in Fig. 5. Quite generally, a given potential  $\psi$  generates a  $B$  mode with  $Q + iU = -i\bar{\partial}^2 \psi$  and  $Q - iU = i\bar{\partial}^2 \psi$ , and an  $E$  mode with  $Q + iU = \bar{\partial}^2 \psi$  and  $Q - iU = \bar{\partial}^2 \psi$ . Since  $i = e^{2i\pi/4}$ , the  $B$ -mode polarization pattern is obtained from the  $E$  mode by rotating by  $45^\circ$  about the line of sight.

*Statistics of CMB polarization.* The decomposition of the polarization field into  $E$  and  $B$  parts is invariant under rotations, and the  $E$  and  $B$  multipoles transform like

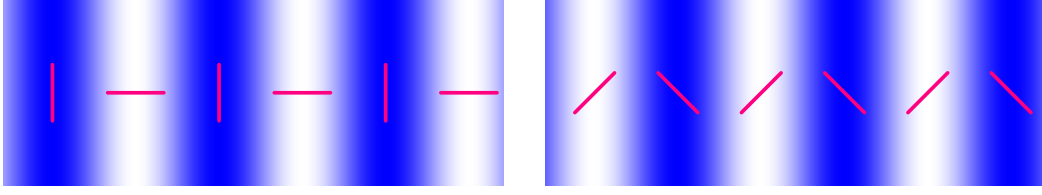


**FIGURE 5.** Polarization patterns for an  $E$  mode (left) and  $B$  mode (right) on a small patch of the sky for potentials that are locally Fourier modes. The shading denotes the amplitude of the potential and the headless vectors denote the unsigned direction of the polarization. For the electric pattern the polarization is aligned with or perpendicular to the Fourier wavevector depending on the sign of the potential; for the magnetic pattern the polarization is at 45 degrees.

those for the temperature anisotropies, e.g.  $E_{lm} \rightarrow \sum_{m'} D_{mm'}^l E_{lm'}$ . Under the operation of parity,  $(Q \pm iU)(\hat{\mathbf{n}}) \rightarrow (Q \mp iU)(-\hat{\mathbf{n}})$  so that  $E_{lm} \rightarrow (-1)^l E_{lm}$  (electric parity) while  $B_{lm} \rightarrow (-1)^{l+1} B_{lm}$  (magnetic parity).

Rotational and parity invariance in the mean limit the non-zero two-point correlations between polarization (and temperature) multipoles to

$$\langle E_{lm} E_{l'm'}^* \rangle = \delta_{ll'} \delta_{mm'} C_l^E \quad (53)$$

$$\langle B_{lm} B_{l'm'}^* \rangle = \delta_{ll'} \delta_{mm'} C_l^B \quad (54)$$

$$\langle T_{lm} E_{l'm'}^* \rangle = \delta_{ll'} \delta_{mm'} C_l^{TE}, \quad (55)$$

which define the power spectra  $C_l^E$ ,  $C_l^B$  and  $C_l^{TE}$ . Note that there is no correlation between  $B$  and either  $\Delta T$  or  $E$ .

Assuming Gaussian statistics, the cosmic variance in the polarization (auto-)power spectra are

$$\text{var}(\hat{C}_l^E) = \frac{2}{2l+1} (C_l^E)^2, \quad \text{var}(\hat{C}_l^B) = \frac{2}{2l+1} (C_l^B)^2. \quad (56)$$

For the cross-spectrum, the cosmic variance is only slightly more complicated [45, 46]:

$$\text{var}(\hat{C}_l^{TE}) = \frac{1}{2l+1} [(C_l^{TE})^2 + C_l^T C_l^E]. \quad (57)$$

The second term arises from chance correlations between  $\Delta T$  and  $E$  in the single realisation of the sky that we have available. It is the only term present in the cosmic variance of estimators for the cross-spectra that vanish in the mean by parity,  $C_l^{TB}$  and  $C_l^{EB}$ . Due to the presence of correlations between the temperature and the electric polarization, estimates of  $C_l^T$  and  $C_l^E$  have non-vanishing covariance, and each is also correlated with the estimator for  $C_l^{TE}$ ; see [45, 46] for details.

The form of the higher-order polarization spectra implied by rotational invariance in non-Gaussian theories is similar to that for temperature and is described in [55].

## 3.2. Thomson scattering and free-streaming

Polarization is generated by scattering the quadrupole of the temperature anisotropy around recombination and reionization. Prior to recombination, on scales larger than the mean-free path, Thomson scattering keeps the CMB radiation very nearly isotropic in the rest-frame of the baryons, and therefore unpolarized. It is only as the mean-free path grows as recombination is approached that the radiation can free-stream over an appreciable fraction of a wavelength of the perturbations between scatterings and so generate a temperature quadrupole. Subsequent scattering of this quadrupole generates linear polarization. After the CMB last scatters around recombination, the polarization is preserved until further scattering at reionization (see Sec. 3.3).

Thomson scattering changes the linear polarization state of the radiation as [43]<sup>3</sup>

$$d(Q \pm iU) = \dot{\tau} d\eta (Q \pm iU)(\mathbf{e}) - \frac{3}{5} \dot{\tau} d\eta \sum_{|m| \leq 2} \left( E_{2m} - \frac{1}{\sqrt{6}} \Theta_{2m} \right)_{\pm 2} Y_{2m}(\mathbf{e}) \quad (58)$$

Here,  $\Theta_{lm}$  are the multipoles of the fractional temperature fluctuation,  $\Theta(\eta, \mathbf{x}, \mathbf{e}) = \sum_{lm} \Theta_{lm}(\eta, \mathbf{x}) Y_{lm}(\mathbf{e})$ , and, recall,  $\dot{\tau} = -an_e \sigma_T$ . The first term arises from scattering out of the beam and reduces the polarization. The second term, arising from in-scattering, involves the quadrupoles of the temperature anisotropies and the  $E$ -mode polarization. In particular, scattering of unpolarized radiation generates linear polarization  $d(Q + iU) = \dot{\tau} d\eta \bar{\delta}^2 (\sum_m \Theta_{2m} Y_{2m}) / 20$  which is an  $E$ -mode quadrupole. However, the polarization does not generally remain in this state in the presence of spatial inhomogeneities in the polarization induced over the last scattering surface. To see how this works, it is simplest to consider the important cases of density perturbations and gravitational waves separately.

### 3.2.1. Density Perturbations

Density perturbations transform as scalars under reparameterisation of spatial coordinates. In Fourier space, this means that every perturbed tensor is azimuthally-symmetric about the wavevector  $\mathbf{k}$ . The same is true of the temperature fluctuation and so for the

---

<sup>3</sup> When discussing the production and propagation of polarized radiation, it is convenient to associate the radiation with the point  $\mathbf{e}$  on the sphere. At this point, the propagation direction is outwards so a right-handed polarization basis is formed by  $\hat{\theta}$  and  $\hat{\phi}$  there; this is equivalent to using  $\hat{\theta}$ ,  $-\hat{\phi}$  at  $\hat{\mathbf{n}} = -\mathbf{e}$  and so the Stokes parameters are the same in both descriptions. However,  $(Q + iU)(\mathbf{e})$  is then spin +2 and its appropriate expansion in spin harmonics is

$$(Q \pm iU)(\mathbf{e}) = \sum_{lm} (E_{lm} \pm iB_{lm})_{\pm 2} Y_{lm}(\mathbf{e}).$$

The multipoles  $E_{lm}$  and  $B_{lm}$  here are related to those in the line-of-sight description by factors of  $(-1)^l$  and  $(-1)^{l+1}$  respectively and so the parity-invariant power spectra are unchanged.

quadrupole we must have

$$\sum_{|m|\leq 2} \Theta_{2m}(\eta, \mathbf{k}) Y_{2m}(\mathbf{e}) \propto P_2(\hat{\mathbf{k}} \cdot \mathbf{e}) = \frac{4\pi}{5} \sum_{|m|\leq 2} Y_{2m}(\mathbf{e}) Y_{2m}^*(\hat{\mathbf{k}}), \quad (59)$$

where, in the second equality, we have used the addition theorem for spherical harmonics. As a concrete example, consider scales which are large compared to the mean-free path  $l_p$ . Applying Eq. (20) over one scattering time, a quadrupole temperature anisotropy builds up most efficiently by the Doppler term. If we locate ourselves at the origin, the temperature anisotropy is

$$\Theta(\eta, \mathbf{0}, \mathbf{e}) \sim \mathbf{e} \cdot \mathbf{v}_b(\eta - l_p, -l_p \mathbf{e}) \approx \mathbf{e} \cdot \mathbf{v}_b(\eta - l_p, \mathbf{0}) - l_p \mathbf{e} \cdot (\mathbf{e} \cdot \nabla \mathbf{v}_b)(\eta - l_p, \mathbf{0}). \quad (60)$$

The quadrupole part of this comes from the last term which, for a single Fourier mode, gives

$$\sum_{|m|\leq 2} \Theta_{2m}(\eta, \mathbf{k}) Y_{2m}(\mathbf{e}) \sim \frac{2}{3} k l_p P_2(\hat{\mathbf{k}} \cdot \mathbf{e}) v_b(\mathbf{k}). \quad (61)$$

Note that this is  $O(kl_p)$  whereas the monopole source terms in Eq. (20) can only produce a quadrupole of  $O(k^2 l_p^2)$ . If we choose coordinates with the  $z$ -axis along  $\mathbf{k}$ , the temperature anisotropies are all in the  $m = 0$  modes for density perturbations.

Scattering of the quadrupole generates  $Q \pm iU \sim \sum_{|m|\leq 2} Y_{2m}^*(\hat{\mathbf{k}})_{\pm 2} Y_{2m}(\mathbf{e})$  locally. If we take  $\mathbf{k}$  along  $z$ , we have  $Q \propto \sin^2 \theta$  and  $U = 0$ . How does the character of the observed polarization change by free-streaming (ignoring reionization for the moment)? What we observe from this single Fourier mode still has  $U = 0$ , but the angular dependence of  $Q$  is further modulated by the spatial dependence of the perturbation over the last-scattering surface. This modulation transfers polarization from  $l = 2$  to higher multipoles (with most appreciable power appearing at  $l = k\chi_*$ ), but preserves the electric character of the polarization [45, 46]. We can see that this is reasonable by noting that the modulated polarization field has its polarization direction either parallel or perpendicular to the direction in which the polarization amplitude is changing [56]. In more detail, if we take  $\hat{\mathbf{k}}$  along the  $z$ -axis, the observed polarization at the origin is

$$(Q \pm iU)(\mathbf{e}) = (Q \pm iU)(\eta_*, -\chi_* \mathbf{e}, \mathbf{e}) \propto (1 - \mu^2) e^{-ik\chi_* \mu}, \quad (62)$$

where  $\mu \equiv \hat{\mathbf{k}} \cdot \mathbf{e} = \cos \theta$ . (Note that  $U$  is zero in this orientation.) Since the polarization is azimuthally symmetric, the same will be true of any  $E$  and  $B$  modes. Taking

$$Q + iU = \bar{\partial}^2(\psi_E + i\psi_B), \quad Q - iU = \bar{\partial}^2(\psi_E - i\psi_B), \quad (63)$$

where  $\psi_E = \sum_{l \geq 2} \sqrt{(l-2)!/(l+2)!} E_{l0} Y_{l0}(\theta, \phi)$  and similarly for  $\psi_B$ , to satisfy Eq. (62) we must have

$$(1 - \mu^2)(\psi_E'' \pm i\psi_B'') \propto (1 - \mu^2) e^{-ik\chi_* \mu}, \quad (64)$$

where primes denote differentiation with respect to  $\mu$ . It follows that  $\psi_B = 0$  (the non-zero solutions of  $\psi_B'' = 0$  are combinations of  $l = 0$  and  $l = 1$  modes and cannot generate polarization) so there are no  $B$  modes. Since  $E$  and  $B$  modes transform irreducibly

under rotations, there will be no  $B$  modes for a general  $\mathbf{k}$ . Dropping the proportionality constant, the relevant solution of  $\psi_E'' = e^{-ik\chi_*\mu}$  is  $a_0(k\chi_*) + a_1(k\chi_*)\mu - e^{-ik\chi_*\mu}/(k\chi_*)^2$  where  $a_0$  and  $a_1$  should be chosen to remove the  $l = 0$  and  $l = 1$  modes. Expanding the exponential gives

$$E_{l0} = -(-i)^l \sqrt{4\pi} \sqrt{2l+1} \sqrt{\frac{(l+2)!}{(l-2)!}} \frac{j_l(k\chi_*)}{(k\chi_*)^2}. \quad (65)$$

The multipoles for a general direction of  $\hat{\mathbf{k}}$  can be found by the appropriate rotation. Note that the spatial-to-angular projection of scalar polarization is controlled by the same function,  $j_l(k\chi_*)/(k\chi_*)^2$ , as for the temperature anisotropies from gravitational waves (see Eq. (45)).

The polarization power spectra produced by adiabatic density perturbations are plotted in the left panel of Fig. 4. They were computed with the Boltzmann code CAMB [38]. The  $E$ -mode power peaks around  $l \sim 1000$ , corresponding to the angle subtended by the width of the visibility function at recombination. On larger scales the polarization probes the electron-baryon velocity at last scattering, as described above. Acoustic oscillations of the plasma prior to last scattering imprint an oscillatory structure on the angular power spectra of the CMB observables. Asymptotically, the photon-baryon overdensity oscillates as a cosine, and the peculiar velocity of the plasma as a sine, to satisfy the continuity equation. The peaks in the  $E$ -mode spectrum therefore coincide with the troughs of the temperature spectrum. Note also that the temperature and  $E$ -mode polarization are correlated [57] and that modes caught at either the midpoint or extrema of their oscillation at last scattering give zeroes in the temperature-polarization cross-correlation. Large-angle polarization from the last-scattering surface is very small since the generation of a quadrupole in the temperature anisotropy occurs via causal physics (photon diffusion) that is suppressed outside the horizon. The increase in polarization on large scales in Fig. 4 is due to reionization [6] and is discussed further in Sec. 3.3.

### 3.2.2. Gravitational Waves

For gravitational waves, a temperature quadrupole builds up over a scattering time due to the shear of the gravitational wave:

$$\Theta(\mathbf{e}) \sim -\frac{1}{2} l_p \dot{h}_{ij} e^i e^j. \quad (66)$$

Consider a circularly-polarized gravitational wave with  $\mathbf{k}$  along the  $z$ -axis so that the temperature quadrupole is a  $|m| = 2$  mode. Equations (43) and (58) show that Thomson scattering of this temperature quadrupole produce polarization that locally has

$$Q \pm iU \sim l_p \dot{h}^{(p)}(k\hat{\mathbf{z}}) \frac{1}{20} \sqrt{\frac{8\pi}{5}} {}_{\pm 2}Y_{2p}(\mathbf{e}), \quad (67)$$



where  $h^{(p)}(\mathbf{k})$  is the Fourier amplitude of the gravitational wave with  $p = \pm 2$  labelling the helicity.<sup>4</sup> Unlike scalar perturbations, the local polarization has both  $Q$  and  $U$  non-zero and modulating these with the plane wave  $e^{-i\chi_* \mathbf{k} \cdot \mathbf{e}}$  will produce both  $E$  and  $B$ -mode polarization [45, 46]. In detail, the observed polarization is

$$\begin{aligned}
(Q \pm iU)(\mathbf{e}) &\propto {}_{\pm 2}Y_{2p}(\mathbf{e})e^{-ik\chi_* \cos \theta} \\
&= {}_{\pm 2}Y_{2p}(\mathbf{e}) \sum_L \sqrt{4\pi} \sqrt{2L+1} (-i)^L j_L(k\chi_*) Y_{L0}(\mathbf{e}) \\
&= \sqrt{5} \sum_L \left[ \sqrt{2L+1} (-i)^L j_L(k\chi_*) \right. \\
&\quad \left. \times \sum_l \sqrt{2l+1} \begin{pmatrix} 2 & L & l \\ -p & 0 & p \end{pmatrix} \begin{pmatrix} 2 & L & l \\ \pm 2 & 0 & \mp 2 \end{pmatrix} {}_{\pm 2}Y_{lp}(\mathbf{e}) \right] \\
&= -\sqrt{5} \sum_l (-i)^l \sqrt{2l+1} {}_{\pm 2}Y_{lp}(\mathbf{e}) \left[ \varepsilon_l(k\chi_*) \pm \frac{p}{2} i\beta_l(k\chi_*) \right], \quad (68)
\end{aligned}$$

where we have used an addition theorem for the spin spherical harmonics, and the functions

$$\varepsilon_l(x) \equiv \frac{1}{4} \left[ \frac{d^2 j_l(x)}{dx^2} + \frac{4}{x} \frac{dj_l(x)}{dx} + \left( \frac{2}{x^2} - 1 \right) j_l(x) \right], \quad (69)$$

$$\beta_l(x) \equiv \frac{1}{2} \left[ \frac{dj_l(x)}{dx} + \frac{2}{x} j_l(x) \right] \quad (70)$$

follow from substituting the explicit form of the  $3j$  symbols and using the recursion relations for the spherical Bessel functions. Reinstating numerical factors from Eq. (67), and rotating to a general  $\mathbf{k}$ , the non-zero  $E$ - and  $B$ -mode multipoles are

$$E_{lm} = -\frac{\sqrt{2\pi^2}}{5} l_p (-i)^l \dot{h}^{(\pm 2)}(\mathbf{k}) \varepsilon_l(k\chi_*) {}_{\mp 2}Y_{lm}^*(\hat{\mathbf{k}}) \quad (71)$$

$$B_{lm} = \mp \frac{\sqrt{2\pi^2}}{5} l_p (-i)^l \dot{h}^{(\pm 2)}(\mathbf{k}) \beta_l(k\chi_*) {}_{\mp 2}Y_{lm}^*(\hat{\mathbf{k}}). \quad (72)$$

We see that gravitational waves project onto both  $E$ - and  $B$ -mode polarization. The projection from last scattering peaks at multipoles  $l \sim k\chi_*$  and divides power roughly equally between  $E$  and  $B$  [43]. Note also that under a parity transformation,  $\dot{h}^{(\pm 2)}(\mathbf{k}) \rightarrow \dot{h}^{(\mp 2)}(-\mathbf{k})$ . Given that  ${}_s Y_{lm}(-\hat{\mathbf{k}}) = (-1)^l {}_{-s} Y_{lm}(\hat{\mathbf{k}})$ , Eqs (71) and (72) manifestly give  $E_{lm} \rightarrow (-1)^l E_{lm}$  and  $B_{lm} \rightarrow -(-1)^l B_{lm}$ , as required, under parity.

The polarization power spectra from a scale-invariant background of gravitational waves with tensor-to-scalar ratio  $r = 0.22$  is shown in the right-hand panel of Fig. 4.

---

<sup>4</sup> A more careful treatment of Eq. (40), balancing in- and out-scattering in the presence of the shear source, and properly including the polarization dependence of Thomson scattering, introduces a prefactor of  $10/3$  in these expressions; see [43, 58, 59].

As for temperature anisotropies, the spectra peak on scales corresponding to the horizon size at recombination. Note that the gravitational wave contribution to the temperature anisotropies and electric polarization is sub-dominant to the scalar perturbations, but gravitational waves dominate the  $B$ -mode polarization on large angular scales. (On small scales, the non-linear  $B$ -modes induced by the action of gravitational lensing on the largely  $E$ -mode primary polarization are dominant.) The increase in polarization power on the largest scales in Fig. 4 is due to reionization, which we now briefly discuss.

### 3.3. Polarization from reionization

For polarization, re-scattering suppresses the signal from last-scattering by a factor  $e^{-\tau_{\text{re}}}$  but also produces a new large-angle signal [6] (see Fig. 4). From Eq. (58) we see that the strength of this large-angle polarization varies almost linearly with  $\tau_{\text{re}}$  and the size of the temperature quadrupole at reionization. Since reionization appears to have completed before dark energy came to dominate the expansion, the temperature quadrupole at last scattering is sourced by the Sachs-Wolfe and Doppler effects on the last scattering surface of the re-scattering electron. Therefore, the quadrupole is dominated by modes with  $k(\eta_{\text{re}} - \eta_*) \sim 2$ . After scattering, the newly-generated  $l = 2$   $E$ -mode polarization free-streams to give  $E$ -mode (and, for gravitational waves,  $B$ -mode) polarization that peaks at multipoles  $l \sim 2(\eta_0 - \eta_{\text{re}})/(\eta_{\text{re}} - \eta_*)$ . The position of the reionization feature is thus controlled by the epoch of reionization. The detailed history of reionization does generate some further small features in large-angle polarization but extracting this is rather limited by cosmic variance [60, 61].

Currently WMAP is the only polarized dataset with sufficient sky coverage to extract  $\tau_{\text{re}}$ . The latest results give  $\tau_{\text{re}} = 0.087 \pm 0.017$  [9]. For instantaneous reionization, this limits the redshift  $z_{\text{re}} > 8.2$  at 95% confidence, which, combined with quasar absorption spectra that indicate reionization was complete by  $z = 6$  (e.g. [62]), points to reionization being an extended process. The determination of  $\tau_{\text{re}}$  required aggressive cleaning of polarized Galactic foreground emission by the WMAP team, but their result is stable to variations in the details of the cleaning process [9].

### 3.4. Current measurements of polarization power spectra

In Fig. 6, we show all current measurements of the  $E$ -mode power spectrum and the  $T$ - $E$  correlation. WMAP [29] provides the best measurements on large scales while the recent QUaD data [63] is most constraining on intermediate and small scales. The data is still rather noisy but the qualitative agreement of the polarization spectra to the best-fit  $\Lambda$ CDM model (which is still driven by the higher signal-to-noise temperature data) is striking. This is an important test of the structure formation model: the polarization mainly reflects the plasma bulk velocities around recombination and these are consistent, via the continuity equation, with the density fluctuations that mostly seed the temperature anisotropies. In a more detailed analysis of consistency, carried out in [69], a mild tension is reported between the QUaD data (particularly for  $C_l^{TE}$ ) and the best-fitting

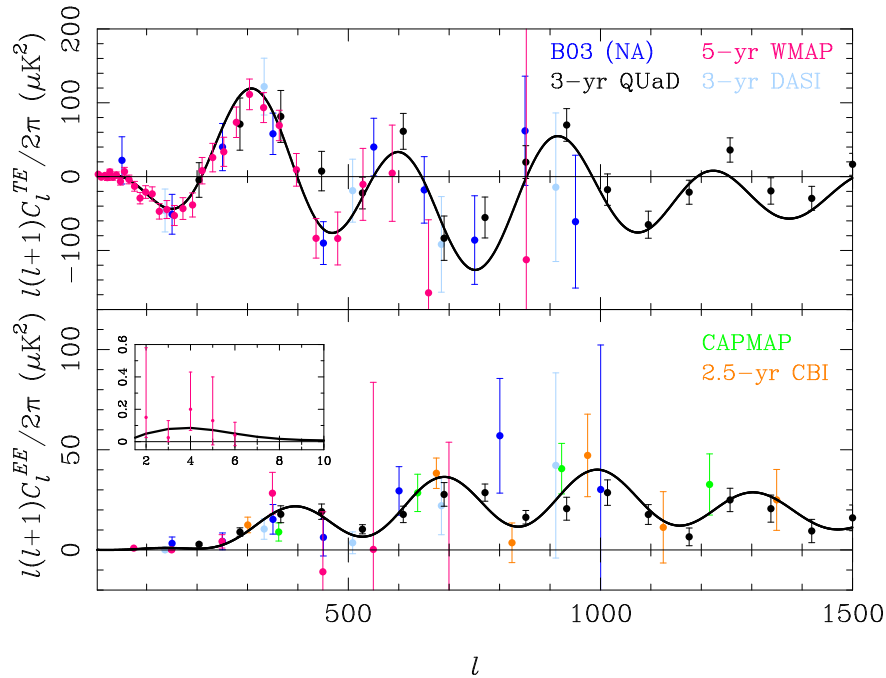


**FIGURE 6.** Current measurements of  $C_l^{TE}$  (top) and  $C_l^E$  (bottom) from WMAP5 (magenta; [29]), QUaD (black; [63]), BOOMERanG (blue; [64, 65]), DASI (cyan; [66]), CAPMAP (green; [67]) and CBI (orange; [68]). The line is the best-fit flat,  $\Lambda$ CDM model to the WMAP5 data.

model to the WMAP data. The amplitude of the measured acoustic oscillations in  $C_l^{TE}$  is rather higher for  $l > 500$  than the best-fit model and this appears to be responsible for a high  $\chi^2$  (probability to exceed of 7%) between the QUaD polarization data and the best-fit model. There will be significant improvements in measurements of the  $E$ -mode power spectra in the next three years, most notably from Planck. In addition, several of the new breed of polarimeters targeting  $B$ -mode polarization have the angular resolution and sensitivity to measure  $E$  modes at high signal-to-noise to  $l \sim 2000$ , but their spectra will likely not be competitive with Planck due to their limited sky coverage. It will be interesting to see if the tension in the QUaD polarization data persists in these future datasets.

## 4. COSMOLOGICAL PARAMETERS FROM THE CMB

In this section we briefly discuss the dependencies of the CMB power spectra on the main cosmological parameters and the current measurements of the parameters via this route. Since the CMB observables are mostly a projection of conditions on the last-scattering surface, parameters can have an influence either through the acoustic physics of the pre-recombination plasma or through the angular diameter distance to last scattering,  $d_A$ . The latter controls the projection of linear distances at recombination to observed angular scales on the sky. We defer discussion of the effect of the primordial power spectra to Sec. 5.1.

The parameters that influence the perturbations up to the time of recombination are only the baryon and CDM densities – given that we know the CMB temperature rather precisely – in models with massless neutrinos. These densities set two length scales, the sound horizon  $r_s$  and the damping scale  $k_D^{-1}$ , and influence the relative heights of the acoustic peaks in the CMB power spectra (see below). The modulation of the peak heights largely determines the densities so that  $r_s$  and  $k_D^{-1}$  become standard rulers at the time of last scattering. The angular scale of the anisotropies depends on the angles that these standard rulers subtend today, and hence on  $d_A$ . The main influence of the geometry of space, dark energy and light (but not massless) neutrinos on the observed anisotropies is through their effect on  $d_A$ . They also have a significant effect on the growth of structure at late times, but this only influences the linear CMB anisotropies through the late-time ISW effect on large scales where cosmic variance is large.

To zero order, the primary CMB anisotropies and polarization determine the physical baryon and CDM densities,  $\Omega_b h^2$  and  $\Omega_c h^2$ , and  $d_A$ . Large-angle polarization further determines the optical depth to reionization. Models with the same values for these parameters, and the same primordial power spectra, produce essentially the same CMB power spectra except on the largest scales [70]. This leads to a very precise *geometric degeneracy* with CMB data alone that can only be broken with external data, e.g. the Hubble constant, luminosity distances from supernovae, and  $d_A(z)$  from the baryon acoustic oscillation (BAO) feature in galaxy clustering, or high-resolution observations of secondary effects in the CMB. A consequence of the geometric degeneracy is that the WMAP data *alone* is consistent with a model with a closed geometry and no dark energy, albeit with a very low Hubble constant (e.g. [71]). There are other *approximate* degeneracies in current CMB data, such as between the shape of the primordial perturbation spectrum (i.e. its spectral index,  $n_s$ ; see Sec. 5.1) and the matter density or the tensor-to-scalar ratio,  $r$ .

## 4.1. Matter composition

The dependence of the temperature and  $E$ -mode polarization power spectra on  $\Omega_b h^2$  and  $\Omega_c h^2$  is illustrated in Fig. 7. The main effects can be understood as follows. Consider increasing  $\Omega_b h^2$  at fixed matter density  $\Omega_m h^2 \equiv \Omega_b h^2 + \Omega_c h^2$ . The increase in baryon inertia reduces the sound speed in the pre-recombination plasma by reducing its bulk modulus. As explained in Sec. 2.5, this shifts the mid-point of the acoustic oscillations to greater overdensities and enhances the height of the compressional peaks ( $n = 1, 3, \dots$  for adiabatic initial conditions) in  $C_l^T$ . The sound horizon is also reduced, shifting the acoustic peaks in temperature and polarization to smaller scales (larger  $l$ ). The increase in the number density of electrons in the plasma reduces the photon mean-free path,  $l_p$ , reducing the amount of diffusion damping and so increasing power on small scales. On larger scales, where tight-coupling still holds approximately, the reduction in  $l_p$  decreases the quadrupole anisotropy around recombination (the reduction in the plasma bulk velocity also contributes the same way) and the polarization is reduced.

Consider instead increasing  $\Omega_m h^2$  at fixed  $\Omega_b h^2$ . At fixed dark energy density and curvature radius, the expansion rate would increase at all redshifts and  $d_A$  would fall.

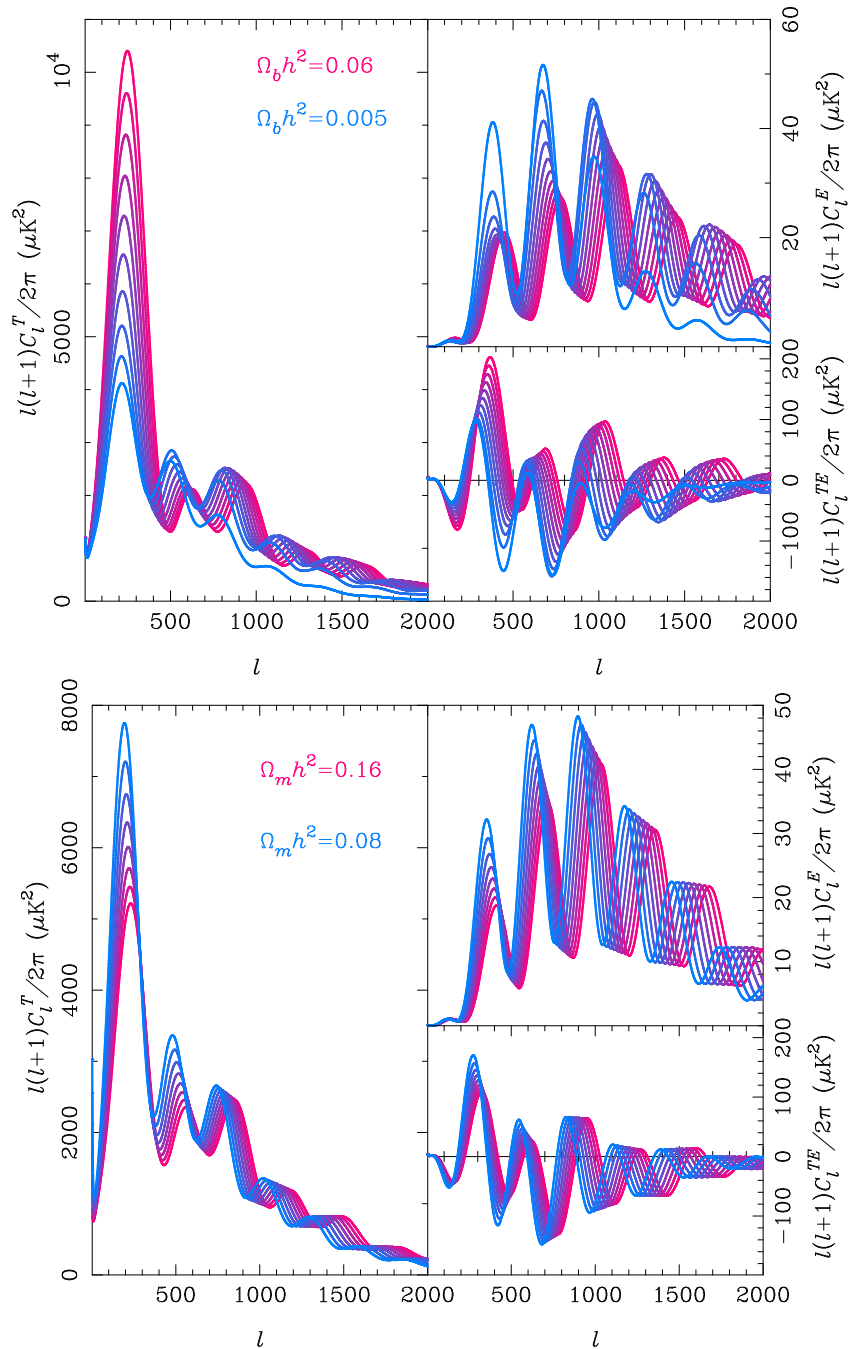


**FIGURE 7.** Variation of  $C_l^T$  (left),  $C_l^E$  (top right) and  $C_l^{TE}$  (bottom right) as  $\Omega_b h^2$  is varied with fixed  $\Omega_m h^2$  (top) and as  $\Omega_m h^2$  is varied at fixed  $\Omega_b h^2$  (bottom). For the latter the angular diameter distance to last scattering has been held fixed. All models are flat.

We have factored this effect out in Fig. 7 by reducing the dark energy density to keep  $d_A$  fixed. The main effects of increasing  $\Omega_m h^2$  are then to push matter-radiation equality back further in time and reduce the sound horizon and diffusion scale (since the

conformal age of the universe is reduced). Since the residual radiation is then lessened at recombination, the early-ISW effect and thus the first peak in  $C_l^T$  are also reduced. The resonant driving effect that enhances the amplitude of the acoustic oscillations for modes that enter the sound horizon during radiation domination is also limited to higher peak order. Together, these effects lead to the relative enhancement of the third and higher peaks over the first two that can be seen in  $C_l^T$  in Fig. 7. The reduction in the sound horizon shifts the temperature and polarization peaks to larger  $l$ . Decreasing diffusion reduces the polarization on large scales where tight-coupling holds, as does the lessened impact of resonant driving.

These effects on the morphology of the acoustic peaks have allowed accurate measurements of the matter and baryon densities from the CMB. Five years of WMAP data alone give  $\Omega_b h^2 = 0.02273 \pm 0.00062$  (i.e. 3% uncertainty) and  $\Omega_c h^2 = 0.1099 \pm 0.0062$  (and so  $\Omega_m h^2 = 0.1326 \pm 0.0063$ ; 6% uncertainty) in flat  $\Lambda$ CDM models [9]. These numbers should improve to sub-percent levels with better measurements of the third and higher peaks with the Planck data in the future [4].

Neutrino oscillations imply that at least two flavours are massive (see [72] for a review in the cosmological context). The minimum mass of the heaviest eigenstate is  $\approx 0.05$  eV. At this minimum level, neutrinos are still relativistic at recombination and their effect on the dynamics of the primordial plasma are indistinguishable from massless neutrinos. A neutrino is non-relativistic at recombination if its mass exceeds  $\approx 0.6$  eV. At this mass, the eigenstates must be very nearly degenerate and the total (summed) neutrino mass is therefore  $\sum_\nu m_\nu \approx 1.8$  eV. This sets a rough limit on the determination of masses from the primary CMB anisotropies and is close to the limit  $\sum_\nu m_\nu < 1.3$  eV from the five-year WMAP data alone in flat,  $\Lambda$  models [44]. Even with minimal masses, two of the neutrino eigenstates are non-relativistic today and therefore affect  $d_A$  and suppress the late-time growth of structure on scales small enough that the neutrinos cannot cluster. The former effect can be used to improve constraints on  $\sum_\nu m_\nu$  from the CMB if external data is used to break the geometric degeneracy. In WMAP5, the constraint on  $\sum_\nu m_\nu$  improves to 0.67 eV in flat,  $\Lambda$  models by including supernovae and BAO distance data. The effect of sub-eV neutrinos on structure formation affects the lensing of the CMB by large-scale structure, making CMB lensing a promising technique for determining masses (see Sec. 6.1.2).

## 4.2. Geometry and dark energy

Generalising our discussion of flat models in Sec. 2.5 to non-flat models, the positions of the acoustic peaks in models with adiabatic initial conditions are asymptotically at  $l = n\pi d_A / r_s(\eta_*)$  since curvature is never dynamically important before recombination. In flat models, note that  $d_A$  reduces to  $\chi_*$ , the comoving distance to last scattering. With the sound horizon determined from the peak morphology, the CMB alone can be used to measure  $d_A$ : constraints from WMAP5 give  $d_A = 14.1 \pm 0.2$  Gpc in their most general open models with dynamical dark energy [44].

The dependence of  $C_l^T$  on the curvature fraction,  $\Omega_K$  (i.e. the ratio of the current Hubble radius to curvature radius and defined to be positive/negative for open/closed

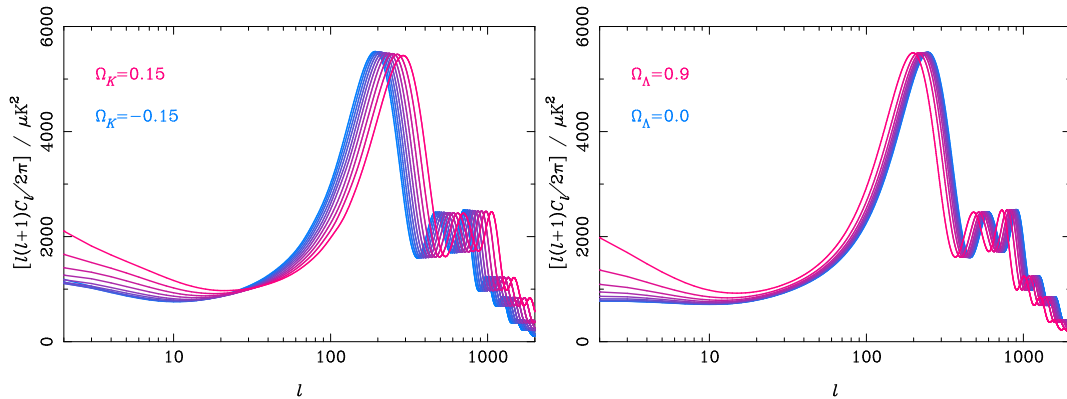


**FIGURE 8.** Variation of  $C_l^T$  with spatial curvature (left) and dark energy density (right). In both cases,  $\Omega_b h^2$  and  $\Omega_c h^2$  are fixed and the dark energy model is a cosmological constant.

models), and dark energy density in  $\Lambda$ CDM models is illustrated in Fig. 8. Both parameters principally affect the anisotropies through  $d_A$  and so simply shift the peaks. The remaining effect on large scales is due to the late-time ISW effect and, in closed models, from mode quantisation. Disentangling the effects of dark energy and curvature from the linear CMB anisotropies requires external data to break the geometric degeneracy. Combining WMAP5 with BAO and supernova data gives  $-0.0178 < \Omega_K < 0.0066$  in  $\Lambda$  models, fully consistent with flatness. (Only one external dataset is required in this case; BAO is the most constraining.) The geometric degeneracy also limits constraints from the CMB alone on more complex models with dynamical dark energy, even for a flat universe; a detailed discussion is given in [44]. The current constraints combining WMAP with *both* BAO and supernova data are consistent with flatness and non-dynamical dark energy: the equation of state parameter  $w$  is consistent with  $-1$  at the 15% level.

## 5. CONSTRAINING EARLY-UNIVERSE PHYSICS WITH THE CMB

### 5.1. Inflation and the origin of structure

So far, we have not discussed the origin of the primordial perturbation which provided the seeds for cosmological structure formation under the action of gravitational instability. The study of this question has the potential to expose deep connections between cosmology and physics at immensely high energies which are forever beyond the reach of earth-bound particle accelerators. Inflation [73, 74, 75, 76, 77, 78], an epoch in which the expansion of the universe is accelerating, solves a number of puzzles associated with the standard big bang cosmology. During a phase of accelerated expansion,  $H^{-1}$  (the physical Hubble radius) remains almost fixed but the physical separation of particles initially in causal contact grows exponentially. The result is that regions today separated by cosmological distances were actually in causal contact before/during inflation. At that time, these regions were given the necessary initial conditions, smoothness

and *small perturbations about smoothness*, we observe today.

The big bang puzzles (e.g. horizon problem, flatness problem, homogeneity problem and monopole problem) are not strict inconsistencies in the standard big bang theory, but must instead be *assumed* as extreme fine-tuning of the initial conditions, thus severely restricting the predictive power of the theory. Inflation provides a *dynamical* mechanism to solve the big bang problems. At the heart of the inflationary paradigm is an elegantly simple idea: *invert the behaviour of the comoving Hubble radius* i.e. make it *decrease* sufficiently in the very early universe. It is easy to see from the second Friedmann equation that the three equivalent conditions necessary for inflation are decreasing comoving Hubble radius, accelerated expansion, and violation of the strong energy condition (i.e. negative pressure):

$$\frac{d}{dt} \left( \frac{H^{-1}}{a} \right) < 0 \quad \Rightarrow \quad \frac{d^2 a}{dt^2} > 0 \quad \Rightarrow \quad \rho + 3p < 0. \quad (73)$$

The requirement for negative pressure means that inflationary dynamics cannot be achieved via normal matter or radiation! Inflation can be phenomenologically described by a scalar field with special dynamics, evolving in a self-interaction potential. Although no fundamental scalar field has yet been detected in experiments, there are fortunately plenty of such fields in theories beyond the standard model of particle physics. Can a scalar field have  $\rho + 3p < 0$ ? The equation of state for a homogeneous scalar field  $\Phi$ ,

$$w = \frac{p}{\rho} = \frac{(\partial_t \Phi)^2/2 - V}{(\partial_t \Phi)^2/2 + V}, \quad (74)$$

shows that a scalar field can lead to accelerated expansion ( $w < -1/3$ ) if the potential energy  $V$  dominates over the kinetic energy  $(\partial_t \Phi)^2/2$ . The equation of motion of such a homogeneous scalar field is

$$\partial_t^2 \Phi + 3H \partial_t \Phi + V_{,\Phi} = 0 \quad (75)$$

where  $V_{,\Phi} \equiv dV/d\Phi$ .

In the following discussion, for notational convenience we will set the reduced Planck mass to unity, i.e.  $8\pi G \equiv M_{\text{Pl}}^{-2} \equiv 1$ . As we have seen, inflation occurs if the field is evolving slow enough that the potential energy dominates over the kinetic energy, and in order to solve the classical big bang problems, the second time derivative of  $\Phi$  is small enough to allow this slow-roll condition to be maintained for a sufficient period. Thus, successful inflation requires

$$(\partial_t \Phi)^2 \ll V(\Phi) \quad (76)$$

$$|\partial_t^2 \Phi| \ll |3H \partial_t \Phi|, |V_{,\Phi}|, \quad (77)$$

where the latter condition means the motion is friction dominated, i.e.  $3H \partial_t \Phi \approx -V_{,\Phi}$  from Eq. (75). Satisfying these conditions requires the smallness of two dimensionless



quantities known as *potential slow-roll parameters*

$$\varepsilon_V(\Phi) \equiv \frac{1}{2} \left( \frac{V_{,\Phi}}{V} \right)^2 \quad (78)$$

$$\eta_V(\Phi) \equiv \frac{V_{,\Phi\Phi}}{V}. \quad (79)$$

In the slow-roll regime,  $\varepsilon_V, |\eta_V| \ll 1$ , with background evolution

$$H^2 \approx \frac{1}{3} V(\Phi) \approx \text{const.}, \quad (80)$$

$$\frac{d\Phi}{dt} \approx -\frac{V_{,\Phi}}{3H}, \quad (81)$$

and the spacetime is approximately *de Sitter*, with the scale factor evolving as  $a(t) \sim e^{Ht}$  where the Hubble parameter  $H$  is approximately constant.

Inflation ends when the slow-roll conditions are violated:  $\varepsilon_V(\Phi_{\text{end}}) \approx 1$ . The number of  $e$ -folds before inflation ends is

$$N_e(\Phi) \equiv \ln \frac{a_{\text{end}}}{a} = \int_t^{t_{\text{end}}} H dt \approx \int_{\Phi_{\text{end}}}^{\Phi} \frac{V}{V_{,\Phi'}} d\Phi'. \quad (82)$$

Roughly 60  $e$ -folds of inflation must occur for the classic big bang puzzles to be resolved. The universe must then *reheat*, the energy density in the scalar field being converted to radiation to start off the radiation-dominated era.

Besides solving the big bang puzzles, the decreasing comoving horizon during inflation is the key feature required for the quantum generation of cosmological perturbations. During inflation, quantum fluctuations are generated on sub-Hubble scales and are then stretched out of the Hubble radius by the accelerated expansion. In other words, the superluminal expansion stretches the perturbations to apparently acausal distances. They become classical superhorizon density perturbations which re-enter the Hubble radius in the subsequent non-accelerating evolution and then undergo gravitational collapse to form the large-scale structure in the universe.

To analyse fluctuations during inflation, the inflaton field is split into a homogeneous background  $\bar{\Phi}(t)$  and a spatially varying perturbation  $\delta\Phi(t, \mathbf{x})$ :

$$\Phi(t, \mathbf{x}) = \bar{\Phi}(t) + \delta\Phi(t, \mathbf{x}). \quad (83)$$

Perturbations of the inflaton field value  $\delta\Phi$  satisfy the equation of motion of a harmonic oscillator with time-dependent mass. The quantum treatment of inflaton perturbations therefore parallels the quantum treatment of a collection of one-dimensional harmonic oscillators. Just as zero-point fluctuations of a harmonic oscillator induce a non-zero variance for the oscillation amplitude  $\langle x^2 \rangle$ , the quantum fluctuations of a light scalar field<sup>5</sup> during inflation induce a non-zero variance for the inflaton perturbations [79]. The

---

<sup>5</sup> Such a field has (effective) mass  $V_{,\Phi\Phi} \ll H^2$  which is equivalent to  $|\eta_V| \ll 1$ .

variance of these fluctuations in Fourier space, i.e. the power spectrum, is

$$\mathcal{P}_{\delta\Phi}(k) = \left(\frac{H_k}{2\pi}\right)^2, \quad (84)$$

where the right-hand side is evaluated when the mode exits the Hubble radius. Our Fourier conventions follow those in Sec. 2.4.1. Technically, the field fluctuation here is defined on hypersurfaces with zero intrinsic curvature and, in this gauge, the result is the same as if metric perturbations (i.e. the back-reaction of  $\delta\Phi$  on the spacetime geometry) were ignored.

A pedagogical review of the generation of density (scalar) perturbations is beyond the scope of this article and we direct the interested reader to the comprehensive treatment in Ref. [80]. The quantity we wish to compute is the comoving curvature perturbation  $\mathcal{R}$ , since this is conserved from Hubble exit during inflation to Hubble re-entry during the standard radiation or matter-dominated epochs. With  $\mathcal{R}$  we can reliably compute the primordial fluctuation (in single-field models of inflation) in the radiation era without needing to model the dynamics of the reheating process. During inflation, comoving hypersurfaces have the property that they coincide with the hypersurfaces over which the (total) inflaton  $\Phi$  is homogeneous. These hypersurfaces are not the same as the zero-curvature surfaces on which Eq. (84) holds – there is a time delay between them,  $\delta t = -\delta\Phi/\partial_t\bar{\Phi}$ , such that the evolution of the background  $\bar{\Phi}$  in this time compensates for the perturbation  $\delta\Phi$  to give a smooth total  $\Phi$ . The differential background expansion during this time delay means that the intrinsic curvature of the comoving hypersurfaces is simply  $\mathcal{R} = -H\delta\Phi/\partial_t\bar{\Phi}$ . In this simple class of inflation models, the power spectrum of  $\mathcal{R}$  is thus [81]

$$\mathcal{P}_{\mathcal{R}}(k) = \left(\frac{H^2}{2\pi\partial_t\bar{\Phi}}\right)_{k=aH}^2 \approx \left(\frac{V^3}{12\pi^2 V_{,\Phi}^2}\right)_{k=aH}, \quad (85)$$

where the second equality uses the slow-roll approximations (80) and (81). The efficiency of this mechanism for producing cosmological curvature perturbations depends on both the height of the potential, which determines the expansion rate and hence size of  $\delta\Phi$ , and its slope, which enters through the conversion of inflaton fluctuations to time delays and so curvature.

For gravitational waves, the two polarization modes of the metric perturbations  $h_{ij}$  (see Eq. 37) satisfy the same equation of motion as the perturbations of a massless scalar field. The power spectrum of  $h_{ij}$  is therefore [77, 78, 81]

$$\mathcal{P}_h(k) = 8 \left(\frac{H_k}{2\pi}\right)^2 \approx \frac{2}{3\pi^2} V \Big|_{k=aH}, \quad (86)$$

where the second equality uses the slow-roll approximation. Our Fourier conventions for  $h_{ij}$  are such that the real-space variance of the metric fluctuation is

$$\langle h_{ij}h^{ij} \rangle = \int \mathcal{P}_h(k) d\ln k. \quad (87)$$

Note that the tensor power spectrum depends only on the expansion rate during inflation. The amplitude of the tensor power spectrum relative to the curvature spectrum defines the tensor-to-scalar ratio

$$r \equiv \frac{\mathcal{P}_h(k_*)}{\mathcal{P}_{\mathcal{R}}(k_*)} \approx 8 \left( \frac{V_{,\Phi}}{V} \right)^2 = 16\epsilon_V. \quad (88)$$

Here,  $k_*$  is some (arbitrary) reference scale. As we will explain below, the value of  $r$  is of fundamental importance in the quest to understand the microscopic origin of the inflationary dynamics.

The power spectra in Eqs. (85) and (86) are to be evaluated when a fluctuation with (physical) wavenumber  $k/a$  exits the Hubble radius  $H^{-1}$ . Different scales exit at different times when the inflationary potential  $V(\Phi)$  has slightly different values. This leads to a small (but computable) scale-dependence of the primordial power spectra. In terms of an empirical parameterisation of this weak scale-dependence, the scalar power spectrum can be written in terms of an amplitude  $A_s$  and a spectral index  $n_s$  as

$$\mathcal{P}_{\mathcal{R}}(k) = A_s (k/k_*)^{n_s-1}, \quad (89)$$

both measured at the reference scale  $k_*$ . Similarly, its tensor counterpart can be written as

$$\mathcal{P}_h(k) = A_t (k/k_*)^{n_t}. \quad (90)$$

The deviation from scale invariance ( $n_s = 1$ ,  $n_t = 0$ ) of these power spectra is sensitive to the *shape* of the inflaton potential:

$$n_s - 1 = 2 \frac{V_{,\Phi\Phi}}{V} - 3 \left( \frac{V_{,\Phi}}{V} \right)^2, \quad (91)$$

and

$$n_t = -4 \left( \frac{V_{,\Phi}}{V} \right)^2. \quad (92)$$

The primordial perturbation spectra are rather directly imprinted in the observable CMB angular power spectra. For example, for scalar perturbations, the dominant Sachs-Wolfe contribution to the anisotropies gives  $C_l \propto \mathcal{P}_{\mathcal{R}}(l/d_A)$ , where the  $l$ -dependent proportionality depends on the processing of the primordial perturbations by gravity and acoustic physics. Measurements of the scale-dependence of the primordial power spectra therefore have the power to probe the shape of the inflaton potential  $V(\Phi)$ . Note the consistency relation,  $r = -8n_t$ , in the simple single-field models we are considering so far.

Two important pieces of information about inflation would follow from a detection of  $A_t$ : (1) the energy scale of inflation; and (2) the field variation of the inflaton. The energy scale of inflation  $V^{1/4}$  is proportional to  $A_t^{1/4}$ . Using the measured value for  $A_s$ , this can be expressed in terms of the tensor-to-scalar ratio on CMB scales,  $r$ , as

$$V^{1/4} = 1.06 \times 10^{16} \text{ GeV} \left( \frac{r}{0.01} \right)^{1/4}. \quad (93)$$

To date, high-energy physicists only have two indirect clues about physics at this scale: the apparent unification of gauge couplings, and experimental lower bounds on the proton lifetime, and these energy scales are forever beyond the reach of earth-bound particle accelerators. Thus, if a primordial tensor mode were to be detected, we would be presented with a unique opportunity to use the universe as a high-energy physics laboratory.

From manipulations of Eq. (88) one may derive [82] the following relation between the tensor-to-scalar ratio  $r$  and the distance in inflaton field space between the end of inflation and the point when the scales of CMB fluctuations were created:

$$\frac{\Delta\Phi}{M_{\text{pl}}} \gtrsim \left(\frac{r}{0.01}\right)^{1/2}. \quad (94)$$

Here, we have reinstated the reduced Planck mass. A large tensor amplitude,  $r > 0.01$ , therefore correlates with a super-Planckian field variation during inflation. Super-Planckian field excursions have interesting theoretical implications [83]: to control the shape of the inflaton potential over a super-Planckian range requires the existence of an approximate shift symmetry in the ultraviolet (UV) limit of the underlying particle theory for the inflaton,  $\Phi \rightarrow \Phi + \text{const}$ . In string theory it has only recently become possible to construct controlled large-field inflation models with approximate shift symmetries in the UV [84, 85, 86].

## 5.2. Observable predictions and current observational constraints

The inflationary proposal requires a huge extrapolation of the known laws of physics. In the absence of a complete theory, a phenomenological approach has been commonly employed, where an effective potential  $V(\Phi)$  is postulated. Ultimately,  $V(\Phi)$  has to be derived from a fundamental theory, and significant progress in implementing inflation in string theory has been made in recent years [86]. However, while it is challenging to understand the origin of inflation from a particle physics point of view, it is also a great opportunity to learn about ultra-high-energy physics from cosmological observations.

The simplest inflationary scenarios consist of a single light scalar field with a canonical kinetic term,  $(\nabla\Phi)^2/2$ , in its action. They predict the following observable characteristics.

1. *Flat geometry*, i.e. the observable universe should have no spatial curvature. As we have seen, flatness has been verified at the 1% level by the location, or, better, separation, of the CMB acoustic peaks combined with some low-redshift distance information.
2. *Gaussianity*, i.e. the primordial perturbations should correspond to Gaussian random variables to a very high precision.
3. *Scale-invariance*, i.e. to a first approximation, there should be equal power at all length-scales in the perturbation spectrum, without being skewed towards high or low wavenumbers. In terms of the parameterisation (89) and (90) this corresponds

to  $n_s = 1$  and  $n_t = 0$ . However, small deviations from scale-invariance are also a typical signature of inflationary models and tell us about the dynamics of inflation.

4. *Adiabaticity*, i.e. after reheating, there are no perturbations in the relative number densities of different species on super-Hubble scales (so no isocurvature modes). This follows from the assumption that only a single field is important during inflation. Constraints on isocurvature modes were discussed in Sec. 2.7.4 where we noted that current data shows no evidence for a non-adiabatic component of the primordial perturbation.
5. *Super-Hubble fluctuations*, i.e. there exist correlations between anisotropies on scales larger than the apparent causal horizon, beyond which two points could not have exchanged information at light-speed during the history of a non-inflationary universe. This corresponds to angular separations on the sky larger than  $\sim 2^\circ$ .
6. *Primordial gravitational waves*, which give rise to temperature and polarization anisotropies as described above. These tensor modes must exist; however, their predicted amplitude can vary by many orders of magnitude depending on the underlying microphysical mechanism implementing inflation.

It is beyond the scope of these lecture notes to describe in algorithmic detail how CMB observations can be used to constrain inflationary physics; the interested reader is referred to Ref. [87] for a beginner-level introduction and a guide to the primary literature. The tightest constraints on inflationary physics currently come from the WMAP data in combination with complementary cosmological data. We now summarise some of the main consequences of the five-year data for inflation where these have not been covered elsewhere in these notes.

### 5.2.1. Super-horizon correlations

The WMAP detection of an (anti-)correlation between CMB temperature and polarization fluctuations at angular separations  $5^\circ > \theta > 1^\circ$  (corresponding to the  $TE$  anti-correlation seen for multipoles  $l \sim 50\text{--}150$  in Fig. 6) is a distinctive signature of adiabatic fluctuations on super-horizon scales at the epoch of recombination, confirming a fundamental prediction of the inflationary paradigm [57, 88, 89]. Inflation, in which microscopic quantum fluctuations are stretched to super-Hubble scales, is the most compelling causal mechanism for generating such apparently-acausal perturbations. The observed  $TE$  anti-correlation on large scales is remarkable qualitative evidence for this basic mechanism.

### 5.2.2. Measurements of the scalar spectrum

Komatsu et al. [44] recently used the WMAP five-year temperature and polarization data, combined with the luminosity distance data of Type-Ia supernovae (SN) at redshifts  $z \leq 1.7$  [90] and BAO data at redshifts  $z = 0.2$  and  $0.35$  [91], to put constraints on the shape of the primordial power spectra (see Table 1).

**TABLE 1.** Five-year WMAP constraints on the primordial power spectra in the power-law parameterisation [44].

	5-year WMAP	WMAP+BAO+SN
$n_s$	$0.963^{+0.014}_{-0.015}$	$0.960 \pm 0.013$
$n_s$	$0.986 \pm 0.022$	$0.970 \pm 0.015$
$r$	$< 0.43$	$< 0.22$
$n_s$	$1.031^{+0.054}_{-0.055}$	$1.017^{+0.042}_{-0.043}$
$\alpha_s$	$-0.037 \pm 0.028$	$-0.028 \pm 0.020$
$n_s$	$1.087^{+0.072}_{-0.073}$	$1.089^{+0.070}_{-0.068}$
$r$	$< 0.58$	$< 0.55$
$\alpha_s$	$-0.050 \pm 0.034$	$-0.053 \pm 0.028$

The WMAP analysis employed the standard power-law parameterisation of the scalar power spectrum given in Eq. (89). The amplitude of scalar fluctuations at  $k_* = 0.002 \text{ Mpc}^{-1}$  is measured to be  $A_s(k_*) = (2.445 \pm 0.096) \times 10^{-9}$ . From both numerical simulations and analytical estimates one finds that with this initial amplitude of density fluctuations, there is sufficient time for gravity to form the large-scale structures that we observe today. Assuming *no* tensor perturbations ( $r \equiv 0$ ) the scale-dependence of the power spectrum is

$$n_s = 0.960 \pm 0.013 \quad (r \equiv 0). \quad (95)$$

The scale-invariant Harrison-Zel'dovich-Peebles spectrum,  $n_s = 1$ , is  $3.1\sigma$  away from the mean of the likelihood. Including the possibility of a non-zero  $r$  in the parameter estimation, the marginalised constraint on  $n_s$  becomes

$$n_s = 0.970 \pm 0.015 \quad (r \neq 0). \quad (96)$$

The (slight) worsening of the constraint simply means that there is a degeneracy between  $n_s$  and  $r$ , and the current data cannot simultaneously measure them independently. Since adding tensor perturbations enhances the large-scale power, it can be offset by increasing  $n_s$ .

### 5.2.3. Constraints on the spectrum of tensor perturbations

At current sensitivities, constraints on the amplitude of tensor perturbations are driven by the temperature data. In the future, this situation should change with weight shifting to the *B*-mode of polarization, as discussed later in Sec. 5.3.2. With five years of WMAP data alone, one finds the following upper limit on the tensor-to-scalar ratio:

$$r < 0.43 \quad (95\% \text{ C.L.}). \quad (97)$$

This improves to  $r < 0.22$  (95% C.L.) if SN and BAO data are included. The latter datasets add only geometric information and so are not influenced by tensor perturba-

tions. However, what they do bring is a better determination of the matter density which, through degeneracies, leads to an improvement in  $n_s$  and hence  $r$ . The limit  $r < 0.22$  is close to the fundamental limit, set by cosmic variance, that can be achieved with temperature data alone. Upcoming polarization experiments with sensitivity to  $B$ -modes should improve on this limit by an order of magnitude or more.

#### 5.2.4. Constraints on inflationary models

At the present stage we are still testing basic aspects of the inflationary *mechanism* rather than details of its specific implementation. However, constraints on specific inflationary models have been obtained (see Fig. 9): inflationary models predicting a blue spectrum ( $n_s > 1$ ) are now virtually ruled out; this includes models of hybrid inflation like  $V(\Phi) = V_0[1 + m^2\Phi^2]$ . Assuming that the tensor amplitude is small, the measurement  $n_s < 1$  implies a constraint on the curvature of the inflaton potential,  $V'' < 0$ . Finally, models predicting a very large tensor amplitude are ruled out, e.g.  $V(\Phi) = \lambda\Phi^4$ . In summary, many popular models are still allowed by the data, but an increasing number of models are on the verge of being tested seriously.

### 5.3. Future prospects for constraining early-universe physics with the CMB

There are exciting prospects for improving our understanding of early-universe physics with new CMB data that will be available in the next decade. The Planck satellite [4] will measure the temperature power spectrum over a large range of scales with unprecedented accuracy and resolution. In addition, it will provide greatly improved constraints on  $E$ - and  $B$ -mode polarization. The Planck data will be supplemented by many sub-orbital experiments with a special focus on measurements of the small-scale temperature fluctuations and/or the polarization power spectra. Finally, plans are being made for a next-generation satellite dedicated to the measurement of CMB polarization [83, 99]. Such an experiment proposes to improve the sensitivity to  $B$ -modes by almost two orders of magnitude over the current situation. As we now describe, the combination of this wealth of data will allow detailed tests of the physics of the early universe.

#### 5.3.1. Scalar perturbation spectrum on small scales

The shape of the spectrum of primordial density fluctuations can be an important diagnostic of the inflationary dynamics. Equation (89) is, of course, only a simple parameterisation of the power spectrum in terms of an amplitude  $A_s$  and a spectral index  $n_s$ , both defined at the pivot scale  $k_*$ . This power-law parameterisation may be refined by allowing a non-zero running of the spectral index,  $\alpha_s \equiv dn_s/d\ln k = d^2 \ln \mathcal{P}_{\mathcal{R}}/d(\ln k)^2$ ,

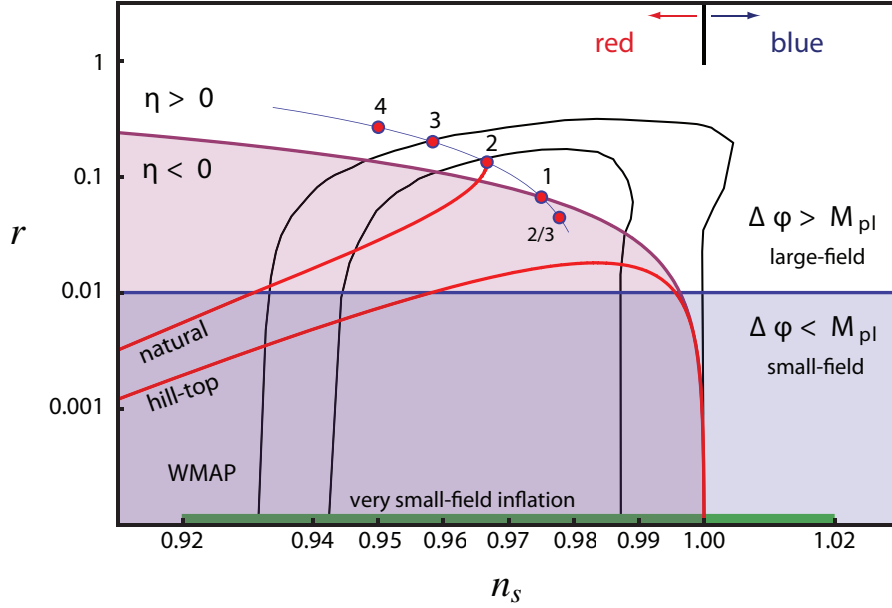


**FIGURE 9.** Constraints on single-field slow-roll models in the  $n_s$ - $r$  plane [83]. The value of  $r$  determines whether the model involves large or small inflaton field variations. The sign of  $n_s - 1$  classifies the scalar spectrum as red or blue. The combination  $2\eta_V = n_s - 1 + 3r/8$  determines whether the curvature of the potential was positive ( $\eta_V > 0$ ) or negative ( $\eta_V < 0$ ) when the observable universe exited the Hubble radius. Shown also are the WMAP five-year constraints on  $n_s$  and  $r$  [44], as well as the predictions of a few representative models of single-field slow-roll inflation: *chaotic inflation* –  $\lambda_p \Phi^p$ , for general  $p$  (thin solid line) and for  $p = 4, 3, 2, 1, 2/3$  (filled circles) – models of which with  $p = 1$  [92] and  $p = 2/3$  [84] have recently been obtained in string theory; *natural inflation* –  $V_0[1 - \cos(\Phi/\mu)]$  (solid line); *hill-top inflation* –  $V_0[1 - (\Phi/\mu)^2] + \dots$  (solid line); *very small-field inflation* – models of inflation with a very small tensor amplitude,  $r \ll 10^{-4}$  (green bar), e.g. brane inflation [93, 94, 95, 96], Kähler inflation [97], and racetrack inflation [98], which often arise in string theory.

i.e. by defining

$$\mathcal{P}_{\mathcal{Q}}(k) = A_s(k_*) \left( \frac{k}{k_*} \right)^{n_s(k_*) - 1 + \alpha_s(k_*) \ln(k/k_*)/2} . \quad (98)$$

Generically, slow-roll inflation predicts that the running should be a small effect, second order in the slow-roll parameters, and so  $|\alpha_s| \sim O(0.001)$ . At present, the data is insufficiently precise to detect  $\alpha_s$  at that level. The current constraints are rather dependent on the combination of CMB data used, and the details of the treatment of contaminants at high multipoles such as emission from extra-Galactic sources and the Sunyaev-Zel'dovich effect in galaxy clusters. Full details can be found in [30, 44]; the basic result is that no running ( $\alpha_s = 0$ ) is consistent with various data combinations at the 95% confidence level but the mean values of  $\alpha_s$  are persistently negative. The key to improving constraints on running is to increase the lever arm in  $k$ . Future small-scale CMB measurements, possibly combined with large-scale structure surveys, should improve constraints considerably though probably not to the level where the prediction of minimal inflation becomes detectable. Forecasts for Planck suggest  $1\sigma$  (marginalised) errors of 0.005 for  $\alpha_s$  [4].



In the case of slow-roll inflation, a definitive measurement of running of the spectral index,  $\alpha_s \neq 0$ , is a signal that  $\xi_H$ , the third *Hubble slow-roll* parameter (defined in analogy to the first two *potential slow-roll* parameters discussed previously),<sup>6</sup>

$$\xi_H \equiv 4M_{\text{pl}}^4 \left[ \frac{H'(\Phi)H'''(\Phi)}{H^2(\Phi)} \right], \quad (99)$$

played a significant role in the dynamics of the inflaton [100] as the CMB scales exited the Hubble radius. In the context of slow-roll inflation it would be hard to explain a value of  $\alpha_s$  that is either negative or positive but much larger in magnitude than 0.001. The consequences for the physics of inflation differ depending on whether the running is negative or positive, and both options would dramatically complicate the theoretical understanding of inflation.

A large negative running implies that  $\xi_H$  was (relatively) large and positive as the cosmological perturbations were laid down ( $\alpha_s \approx -2\xi_H$  in this limit). It can be shown that  $\xi_H > 0$  generally hastens the end of inflation (relative to  $\xi_H = 0$ ), provided the higher order slow-roll parameters can be ignored. With these assumptions, we find a tight constraint on  $\xi_H$  if we are to avoid a premature end to slow roll, with inflation terminating soon after the observable scales exit the Hubble radius [101, 102, 103, 104]. Thus, a definitive observation of a large negative running would imply that any inflationary phase requires higher order slow-roll parameters to become important after the observable scales leave the Hubble radius [101, 102, 105, 106], multiple fields yielding complicated spectra [107], two or more bursts of inflation [108, 109, 110, 111, 112], or a temporary breakdown of slow roll (such as a feature in the potential) [89, 113, 114, 115, 116, 117, 118]. There have also been proposals for explicit models where a large, transient negative running occurs as a “stringy” signature in multi-throat brane inflation [119, 120, 121].

The current cosmological data disfavour inflationary models with a blue tilt,  $n_s > 1$  [9, 44]; however, a significant parameter space is still allowed where  $n_s < 1$  but with a large positive running (implying a large negative  $\xi_H$ ), which would lead to a strongly blue-tilted spectrum on scales below those of cosmological interest [122]. Again under the hypothesis that this parameterisation can be extrapolated to the end of inflation, we find a class of solutions where  $\varepsilon \rightarrow 0$  as  $H$  remains finite, and the field rolls towards a minimum with a substantial vacuum energy. The perturbation spectrum grows at small scales, possibly diverges, and can lead to over-production of primordial black holes [122, 123, 124, 125, 126, 127, 128, 129, 130, 131, 132, 133], or even the onset of eternal inflation [122, 134, 133]. Consequently, if we measure a large positive running we will again conclude that any inflationary phase is not described within the single field, slow-roll formalism, or that higher order terms in slow roll are important.

---

<sup>6</sup> The primes here denote derivatives with respect to  $\Phi$ .

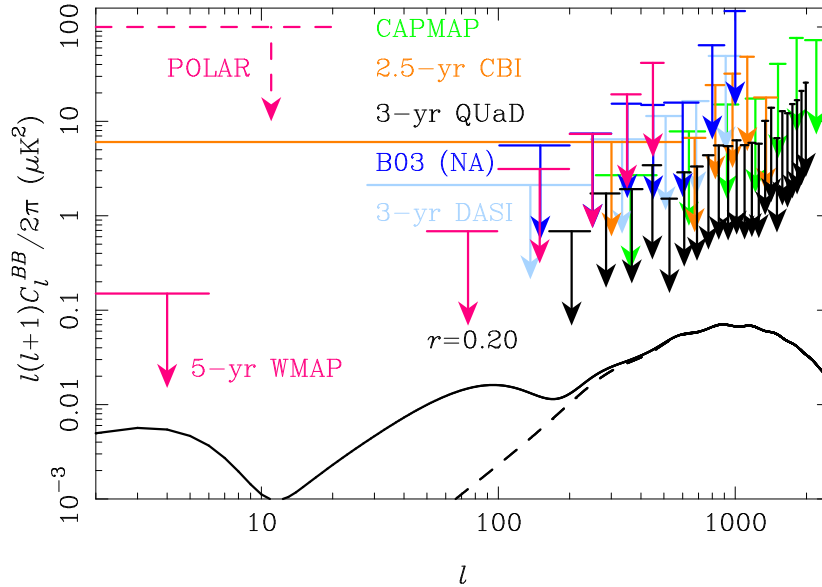


**FIGURE 10.** Current 95% upper limits on  $C_l^B$  from WMAP5 (magenta; [29]), QUaD (black; [63]), BOOMERanG (blue; [64, 65]), DASI (cyan; [66]), CAPMAP (green; [67]), CBI (orange; [68]) and POLAR (dashed magenta; [135]). The solid line is the contribution from gravitational waves for a tensor-to-scalar ratio  $r = 0.2$ . The dashed line is the  $B$ -mode power induced by weak gravitational lensing.

### 5.3.2. Tensor perturbations

The WMAP upper limit on the amplitude of primordial tensor fluctuations,  $r < 0.22$ , is only beginning to be a serious constraint on inflationary model-building. As noted above, current constraints are driven by the large-angle temperature data, but this route is fundamentally limited by the cosmic variance of the dominant scalar perturbations. The same is true for  $E$ -mode polarization but not for  $B$ -mode polarization since this is not generated by scalar perturbations in linear theory. Improved constraints on  $B$ -modes of CMB polarization will therefore drive future limits on the tensor amplitude. The quest for a  $B$ -mode detection is one of the most exciting developments in observational cosmology.

Current limits on  $B$ -mode power are compared in Fig. 10 to the power expected for  $r = 0.2$ . (The secondary contribution from conversion of  $E$  modes to  $B$  by weak gravitational lensing is also shown; see Sec. 6.1.2.) The primordial signal is very weak, with r.m.s. =  $0.18\sqrt{r/0.2}\mu\text{K}$ , but there are no fundamental technical or cosmological obstacles to achieving  $r \sim 0.001$ , although it calls for arrays of thousands of detectors. However, it is still unclear whether polarized Galactic emission, particularly thermal dust emission, is sufficiently well behaved to allow its removal down to this level on the basis of multi-frequency data. There are two characteristic scales for attempting detection. The reionization signal at  $l < 10$ , and the signal from recombination at  $l < 100$ . Where most information lies depends on the value of  $r$ , the instrument sensitivity, the scale-

dependence of Galactic foregrounds, and the size of the survey (i.e. whether the large-scale reionization modes are accessible). Realistic forecasts for Planck suggest  $r = 0.05$  may be achievable, and the constraint is driven by the reionization signal [136]. In contrast, most of the next generation of ground-based and balloon experiments will survey smaller regions of the sky in areas of (known) low foreground contamination, and their target is the signal from recombination [137, 138, 139, 140, 141, 142]. Tensor-to-scalar ratios  $r \sim 0.01$  may be achievable with these surveys. Looking further ahead,  $r \sim 10^{-3}$  with a full-sky survey from a dedicated polarization satellite seems achievable with current technology. Measuring tensors at that level of sensitivity would mark a qualitative shift in our ability to test the inflationary paradigm. If tensors are not seen at that level, all large-field models of inflation are ruled out. On the other hand, a  $B$ -mode detection would be an extraordinary discovery and a “smoking gun” for inflation.

A natural target sensitivity for most future  $B$ -mode experiments is  $\sim 5 \mu\text{K-arcmin}$  in the polarization maps. At this level, the “noise” due to the  $B$  modes produced by gravitational lensing is comparable to the instrument noise [54, 143]. For reference, this is 10 times the sensitivity of the nominal Planck survey. Pushing for further improvements in sensitivity is then only worthwhile if it improves rejection of foreground contamination, or if the lensing contamination can be removed coherently (i.e. at the level of the maps), for example with quadratic reconstruction techniques [144]. Without reconstruction, the ( $3\sigma$ ) upper limits on  $r$  set by lensing, assuming  $r = 0$ , are  $1 \times 10^{-4}$  from the reionization signal and  $8 \times 10^{-4}$  from recombination alone (i.e.  $l > 10$ ). In practice, astrophysical foregrounds and instrumental systematic effects will surely be more of a limitation than lensing noise. Foregrounds will be particularly troubling for the signal from reionization, with estimates suggesting they may limit detections to  $r \sim 0.01$  (99% C.L.) from  $l < 10$  data alone given the frequency coverage and sensitivity being considered for a future satellite mission [145, 146].

### 5.3.3. Non-Gaussianity

So far, we have assumed that the primordial fluctuations have a Gaussian distribution. Indeed, this is a fundamental prediction of slow-roll inflation and the current observational limits confirm this at the 0.1% level.<sup>7</sup> However, as we will now discuss, a small degree of primordial non-Gaussianity can be a crucial probe of the inflationary dynamics.

Non-Gaussianity is a sensitive probe of inflationary physics that is difficult to access by any other means. Specifically, it is a measure of *inflaton interactions*. To allow for slow-roll inflation the inflaton field is necessarily weakly interacting [ $V(\Phi)$  is very flat] and the non-Gaussianity is predicted to be small [147]. However, going beyond the single-field slow-roll paradigm, non-trivial kinetic terms (derivative self-interactions in the inflaton action), the presence of more than one light field during inflation, the (temporary) violation of slow roll, and a non-adiabatic initial vacuum state for the inflaton may lead to large, observationally distinct non-Gaussianity (e.g. [148, 149]).

---

<sup>7</sup> By this measure, non-Gaussianity has been constrained more accurately than curvature.

Gaussian fluctuations are characterised completely by their two-point correlation function, or, equivalently, their power spectrum,  $\mathcal{P}_{\mathcal{R}}(k)$ . Non-Gaussianity is therefore measured by considering the connected higher-order correlation functions, i.e. the part that remains after all possible contractions are subtracted. The connected  $n$ -point functions with  $n > 2$  vanish for a Gaussian random field and so the leading non-Gaussian effect is usually given by the three-point function. To calculate the non-Gaussianity from inflation, generally one must go beyond linear perturbation theory, expanding the action to third order to capture all cubic interactions between perturbed quantities [147]. The primordial 3-point function from inflation is conveniently calculated for quantities  $\zeta$  and  $\gamma_{ij}$  which are the non-linear generalisations of  $\mathcal{R}$ , the linear-theory comoving-gauge curvature perturbation, and  $h_{ij}$ , the linear-theory gravitational wave amplitude, respectively.<sup>8</sup> Both  $\zeta$  and  $\gamma_{ij}$  are conserved on super-Hubble scales in the simplest inflation models. The bispectrum for  $\zeta$  is defined by

$$\langle \zeta(\mathbf{k}_1) \zeta(\mathbf{k}_2) \zeta(\mathbf{k}_3) \rangle = B_{\zeta}(k_1, k_2, k_3) \delta(\mathbf{k}_1 + \mathbf{k}_2 + \mathbf{k}_3). \quad (101)$$

Three other bispectra with different combinations of  $\zeta$  and  $\gamma_{ij}$  can also be constructed. Note that the bispectrum depends only on the magnitudes of the three wavevectors as a consequence of translational, rotational and parity invariance.

The bispectrum is measured by sampling *triangles* in Fourier space. Much physical information is contained in the momentum dependence or the shape of the bispectrum. Ref. [150] presents visualisations of the full scale/shape dependence of the bispectra for a variety of inflationary scenarios in which significant (observable) amounts of non-Gaussianity could be potentially produced. While these have complex shapes, fortuitously, different physical mechanisms that produce significant non-Gaussianity result in bispectrum signals that peak on different triangular configurations (e.g. [48, 149, 151, 152, 153, 154]):

- multi-field models peak on squeezed triangles ( $k_3 \ll k_2 \sim k_1$ );
- models with non-canonical kinetic terms peak on equilateral triangles ( $k_1 \sim k_2 \sim k_3$ );
- models with non-adiabatic initial vacua peak on flattened/folded triangles ( $k_3 \sim k_2 \sim 2k_1$ ); and
- non-slow-roll models peak on more complex (model dependent) configurations requiring a matched template for their analysis.

Thus, configuration-dependent studies of non-Gaussianity may become a powerful probe of ultra-high-energy physics and inflation.

Given a primordial bispectrum, how do we compute the observable bispectrum,  $B_{l_1 l_2 l_3}$ , in the CMB (see Eq. 8)? In theories with weak primordial non-Gaussianity, such as

---

<sup>8</sup> These quantities are defined so that the induced line element on comoving hypersurfaces, over which  $\delta\Phi = 0$ , is [147]

$${}^3g_{ij}dx^i dx^j \equiv a^2 e^{2\zeta} e^{\gamma_{ij}}. \quad (100)$$

Here,  $\gamma_{ij}$  is trace-free and transverse,  $\partial_i \gamma^i_j = 0$ , so that  $\det e^{\gamma_{ij}} = 1$ . Note that the true curvature perturbation of comoving hypersurfaces differs from  $\zeta$  by terms quadratic in  $\zeta$  and  $\gamma_{ij}$ .

single-field inflation, this is a difficult task since the non-linear perturbation evolution and radiative transfer will induce additional non-Gaussianity in the CMB that exceeds (and distorts) the primordial contribution. Signatures of specific non-linear effects have been computed, but a full calculation is still lacking (see [155, 156, 157, 158, 159, 160, 161] for some recent progress towards this goal). Things are more straightforward, though, if the initial level of non-Gaussianity is large enough, since then one can continue to employ linear perturbation theory to compute the higher-order statistical properties of the CMB, replacing the bispectrum of the linear-theory  $\mathcal{R}$  with  $B_\zeta(k_1, k_2, k_3)$ .

Generalising Eq. (22) to include all sources of anisotropy, the multipoles of the temperature anisotropy,  $T_{lm}$ , can be written in the form

$$T_{lm} = 4\pi i^l \int \frac{d^3k}{(2\pi)^{3/2}} g_l(k) \mathcal{R}(\mathbf{k}) Y_{lm}^*(\hat{\mathbf{k}}) e^{i\mathbf{k}\cdot\mathbf{x}_R} \quad (102)$$

in linear theory with adiabatic perturbations. Here,  $g_l(k)$  is the *temperature transfer function* which linearly relates the observed CMB anisotropy to the primordial curvature perturbation. The observed CMB bispectrum then becomes

$$B_{l_1 l_2 l_3} = \sqrt{\frac{(2l_1+1)(2l_2+1)(2l_3+1)}{4\pi}} \begin{pmatrix} l_1 & l_2 & l_3 \\ 0 & 0 & 0 \end{pmatrix} b_{l_1 l_2 l_3}, \quad (103)$$

where the reduced bispectrum  $b_{l_1 l_2 l_3}$  is [162]

$$b_{l_1 l_2 l_3} = \frac{64}{(2\pi)^{3/2}} \int_0^\infty r^2 dr \int \prod_{i=1}^3 [k_i^2 dk_i g_{l_i}(k_i) j_{l_i}(k_i r)] B_\zeta(k_1, k_2, k_3). \quad (104)$$

As a simple and well-studied example, we consider the local model of primordial non-Gaussianity in which  $\zeta$  is a sum of a Gaussian piece and the square of a Gaussian in real-space:

$$\zeta(\mathbf{x}) = \zeta_G(\mathbf{x}) + \frac{3}{5} f_{\text{NL}} [\zeta_G^2(\mathbf{x}) - \langle \zeta_G^2 \rangle]. \quad (105)$$

The factor of  $3/5$  is conventional and is chosen so that  $-f_{\text{NL}}$  parameterises the quadratic contribution to the gravitational potential  $\phi$  in matter domination (for  $|f_{\text{NL}}| \gg 1$  so further non-linear evolution can be ignored).<sup>9</sup> Single-field, slow-roll inflation with canonical kinetic term approximates to the local model, with a very small primordial  $f_{\text{NL}}$  of the order of the slow-roll parameters, i.e.  $\sim O(0.01)$  [147] (non-linear effects – e.g. in the relation between the gravitational potential and  $\zeta$  – increase the effective observable  $f_{\text{NL}}$  to  $O(1)$ ). Large local non-Gaussianity can be generated in models with multiple fields, such as the curvaton model. The bispectrum in the local model evaluates to

$$B_\zeta(k_1, k_2, k_3) = \frac{3f_{\text{NL}}}{5(2\pi)^{3/2}} \left( \frac{2\pi^2}{k_1^3} \mathcal{P}_{\mathcal{R}}(k_1) \frac{2\pi^2}{k_2^3} \mathcal{P}_{\mathcal{R}}(k_2) + \text{perms} \right). \quad (106)$$

---

<sup>9</sup> Our sign choices and normalisation are consistent with [44]. Note that on large scales, the temperature anisotropies are skewed *negative* by a positive  $f_{\text{NL}}$ .

Significantly, this is factorisable which makes the integration in Eq. (104) easily tractable. Numerical examples of the reduced bispectrum in the local model can be found in Ref. [163]; it displays similar acoustic oscillations to the power spectrum. The best observational constraints on the local form of non-Gaussianity are from the 3-point function of the WMAP5 data. With an optimal weighting of the data, Ref. [164] find no evidence for non-zero  $f_{\text{NL}}$ :  $-4 < f_{\text{NL}} < 80$  (95% C.L.). Planck should improve this constraint with its better measurement of the anisotropies on smaller scales; a detection limit of  $f_{\text{NL}} \sim 5$  is forecasted [163].

## 6. SECONDARY ANISOTROPIES

Secondary anisotropies are generated after recombination. They can arise from gravitational effects (the integrated Sachs-Wolfe effect or gravitational lensing) and from scattering events during or after the epoch of reionization. We have already met some examples, such as the large-angle polarization generated from scattering at reionization (Sec. 3.3). In this section we briefly review the other main sources of secondary anisotropy and their cosmological potential. For a recent, thorough review of the subject, see [13]. Fully exploiting the primary anisotropies on multipoles  $l \sim 2000$ , for example to tighten constraints on  $n_s$ , requires careful modelling of secondary effects. Such modelling is also important since the secondary signals themselves contain valuable cosmological information about structure formation at late times and reionization. A number of ongoing ground-based surveys with arcmin resolution are seeking to exploit the secondary anisotropies in this way [165, 166, 167, 168].

### 6.1. Gravitational secondary effects

#### 6.1.1. Integrated Sachs-Wolfe effect

The integrated Sachs-Wolfe (ISW) effect is described by the last term on the right of Eq. (14). It is an additional source of anisotropy due to the temporal variation of the gravitational potentials along the line of sight. If a potential well were to deepen as a photon crossed it, the photon would receive a net redshift, and there would be a decrement to the CMB temperature along the line of sight. Conversely, a decaying potential well gives a temperature increment. At late times, the potential evolves only when dark energy (or curvature) start to dominate the background dynamics – a linear-theory effect – or as non-linear structures form.

The linear effect from evolving potentials contributes to the temperature anisotropies only on large scales (see Fig. 11). This is because there is little power in the gravitational potentials today on scales that entered the Hubble radius during radiation domination, and, furthermore, as an integrated effect, the contribution of small-scale fluctuations is suppressed. The physics of dark energy affects the decay of the potential through the background expansion rate (via its energy density and equation of state) and through its clustering properties (i.e. sound speed). Both impact on the amplitude and detailed scale-dependence of the ISW contribution [169]. The late-time ISW effect is the only

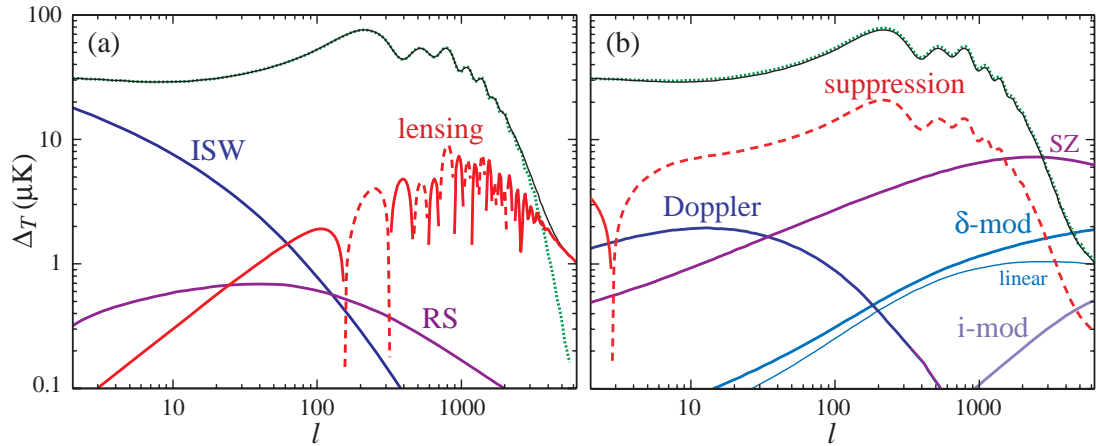


**FIGURE 11.** Predicted secondary anisotropies from gravitational effects (left) and scattering effects (right) from [21]. (a) The ISW (blue), Rees-Sciama (purple) and lensing (red; negative where dashed) effects compared to the primary anisotropies from recombination (green) and the sum of primary and gravitational secondaries (black). (b) The  $\approx -\tau_{\text{re}}$  fractional suppression of the primary anisotropies (red; discussed in Sec. 2.7.2), linear Doppler effect (blue), thermal Sunyaev-Zel’dovich effect (purple; calculated in the Rayleigh-Jeans limit), the density-modulated Doppler effect with linear densities (thin cyan) and the total including non-linear modulation e.g. from clusters of galaxies (thick cyan), and the Doppler effect modulated by the patchiness of reionization (“i-mod”; purple) compared with the primary anisotropies (green). The predictions for the SZ effect, non-linear Doppler-modulation and patchy reionization are based on simplified halo models; see [21] for details. The quantity  $\Delta T \equiv \sqrt{l(l+1)}C_l/2\pi$ .

way to probe late-time structure growth with linear CMB anisotropies alone, but this is hampered by cosmic variance on large angular scales. A more promising route is to cross-correlate the CMB with a tracer of large-scale structure [170]. A positive correlation is expected from decaying potentials, and was first detected by correlating the first-year WMAP data with the X-ray background and the distribution of radio galaxies [171]. Since the initial detection, the correlation has been detected with a number of large-scale structure tracers. The most complete analyses to date [172, 173] find  $\sim 4.5\sigma$  detections. The power of the ISW effect in constraining dark energy models is rather limited by chance correlations between the primary CMB and large-scale structure; the total signal-to-noise can never exceed  $\sim 7$ , even for a tracer perfectly correlated with the ISW signal. Current detections provide independent evidence for dark energy, but no evidence for departures from  $\Lambda\text{CDM}$  (i.e. dynamical dark energy).

The non-linear late-time effect is sometimes called the Rees-Sciama effect [14]. It arises from the non-linear growth of structures and, more generally, from the bulk motion of clustered matter. The power spectrum of the Rees-Sciama effect is broad but is a sub-dominant effect on all scales [174]; see Fig. 11.

### 6.1.2. Weak gravitational lensing

Weak gravitational lensing of CMB photons by the large-scale matter distribution at  $z < 10$  has several important effects on the CMB; see [17] for a recent review. The deflection arises from the cumulative effect of large-scale structure along the line of sight. The total deflections are predicted to have an r.m.s.  $\sim 3$  arcmin, and be coherent over scales  $\approx 1^\circ$  (the angle subtended by the typical coherence size of the gravitational potential,  $\sim 10^2$  Mpc, at a comoving radial distance  $\chi_*/2$  where lensing is most efficient). Lensing conserves brightness, simply re-mapping points according to the deflection field. For the temperature anisotropies, this re-mapping leads to a smoothing of the acoustic peaks resulting in fractional changes in  $C_l^T$  of around 10% at the troughs by  $l \sim 2000$ . Moreover, it transfers large-scale power to small scales so that it dominates the primary anisotropies for  $l > 4000$ ; see Fig. 11. The effects in polarization are similar, but with the important addition that  $B$ -mode polarization is generated from  $E$  [175]. This arises since the re-mapping by lensing does not preserve the geometrical relation between polarization direction and the angular variation of the amplitude which defines  $E$ -mode polarization. The resultant  $B$  modes have an almost white spectrum for  $l \ll 1000$  with  $C_l^B \sim 2 \times 10^{-6} \mu\text{K}^2$ ; see Fig. 4. Characterising the  $B$ -mode polarization from lensing is a secondary science goal of upcoming polarization experiments that have gravitational waves as their primary target [176].

As the angular resolution and sensitivities of CMB experiments have improved, it has become important to include the effect of lensing when deriving parameter constraints from CMB temperature data. For example, in the recent analysis of ACBAR data [30], a significantly better fit of  $\Lambda$ CDM models to the data is found when lensing is included. Including the amplitude of the lensing correction as a parameter in the analysis (with a predicted value  $q = 1$ ), gives  $q = 1.23_{-0.76}^{+0.83}$  (95% C.L.).

An additional feature of lensing is that it introduces non-Gaussian signatures in the CMB. Roughly, sub-degree scale CMB features behind a given lens are sheared coherently producing what locally looks like a statistically-anisotropic pattern of Gaussian CMB fluctuations. Averaged over lenses, statistical-isotropy is restored but the lensed CMB becomes non-Gaussian. This non-Gaussianity, manifesting itself as a non-zero trispectrum [32], may be used to reconstruct a noisy estimate of the deflection field (e.g. [177]). The noise arises from both instrument noise and chance alignments in the primary (random) CMB field that mimic the effect of a lens. The more small-scale features in the field being lensed, the better the reconstruction. Current data is too noisy to allow a direct detection of lensing via the reconstruction route. The signal-to-noise can be improved by cross-correlating the reconstruction with a tracer of large-scale structure. [For a high density of sources, the lower (Poisson) noise compensates for the reduced level of correlation.] The lensing effect in the CMB temperature has now been detected at the  $3\sigma$  level in cross-correlation with galaxy surveys [178, 179].

Moving beyond these first detections, the interest in CMB lensing will turn to exploiting it as a probe of the growth of structure; see [176] for a recent overview. In particular, CMB lensing has the potential to provide constraints on dark energy, modifications of gravity, and massive neutrinos that are inaccessible with the primary CMB anisotropies alone. CMB nicely compliments cosmic shear surveys [180] as it probes structure at higher redshift and with quite different systematic effects.



Note finally that since the effect of gravity on photons is achromatic, the frequency dependence of all gravitational secondary anisotropies follows that of the primary anisotropies.

## 6.2. Scattering secondary effects

### 6.2.1. Thermal Sunyaev-Zel'dovich effect

The thermal Sunyaev-Zel'dovich (SZ) effect arises from Compton up-scattering of CMB photons by electrons in hot, ionized gas such as in galaxy clusters [18]; see also [181] for a review. The CMB temperature at the redshift of the cluster is much less than the gas temperature,  $k_B T \sim \text{few keV}$ , so photons gain energy, on average, by scattering. The net fractional change in the effective temperature of the CMB is

$$\Theta(\hat{\mathbf{n}}; \nu) = y(\hat{\mathbf{n}}) \left[ \left( \frac{h\nu}{k_B T_{\text{CMB}}} \right) \coth \left( \frac{h\nu}{2k_B T_{\text{CMB}}} \right) - 4 \right], \quad (107)$$

where the Compton  $y$  parameter is determined by the integral of the gas pressure along the line of sight:  $y(\hat{\mathbf{n}}) \equiv (\sigma_T/m_e c^2) \int p_e dl$  where  $m_e$  is the electron mass. Unlike the gravitational secondaries, the thermal SZ effect has a characteristic frequency dependence – negative below the null at 217 GHz and positive above. For a typical galaxy cluster,  $\Theta \sim 10^{-4}$  around 100 GHz giving a decrement of  $O(100) \mu\text{K}$ . In the Rayleigh-Jeans limit,  $h\nu \ll k_B T_{\text{CMB}}$ , the decrement is independent of frequency:  $\theta(\hat{\mathbf{n}}; \nu) \approx -2y(\hat{\mathbf{n}})$ .

The SZ effect is now routinely detected in targeted observations towards known clusters. A significant feature of the SZ effect is that *the observed temperature change is independent of the redshift of the cluster* making SZ also a promising route to search for high-redshift clusters. Indeed, a number of blind surveys are now underway, e.g. AMI [165], SZA [166], SPT [167] and ACT [168], to do just this. These ground-based instruments, covering a broad spread of frequencies, all have the high resolution ( $\sim 1$  arcmin) required to resolve clusters, and, together, expect to find thousands of clusters. The Planck satellite, despite its poorer resolution, will produce a full-sky catalogue with  $O(1000)$  SZ clusters. Recently, the detection of three previously unknown clusters was reported by the SPT team [182]; these are the first clusters to be found in a blind SZ survey.

Once detected, clusters will be followed-up with redshift measurements to determine cluster counts as a function of redshift,  $d^2N/dz d\Omega$ . This is related to the underlying cosmology through the expansion rate  $H(z)$ , the cluster mass function,  $dn(M, z)/dM$  giving the number density of clusters per mass  $M$  as a function of redshift, and the survey selection function. The mass function depends sensitively on the growth of structure making cluster counts a promising route to improving our understanding of dark energy [183]. However, to achieve this goal, the survey selection function must be very well understood and this depends on the relation between the SZ observables and the cluster mass. Fortunately, the total SZ flux is expected to be a good proxy for the cluster mass, with the two being related by scaling relations. We can see that this is reasonable by noting that the SZ flux is proportional to the volume integral of

the electron pressure, by Eq. (107), and hence electron thermal energy. For a relaxed cluster, the virial theorem relates the thermal energy, hence SZ flux, to the virial mass. For a flux-limited SZ survey, the selection function should be rather uniform in mass. Better understanding the relation between mass and SZ observables, both with further simulation work and X-ray and optical follow-up, is an important aspect of SZ cluster research.

The thermal-SZ effect is an important foreground for studies of the primary CMB temperature anisotropies on small scales. The power spectrum is shown in Fig. 11 in the Rayleigh-Jeans limit. On large scales it is essentially white noise, but turns over on scales where clusters are resolved. Since the frequency spectrum is known, and differs from the primary CMB anisotropies, the thermal SZ effect can be removed with multi-frequency observations or by observing close to the null at 217 GHz. Moreover, the signal is very non-Gaussian. However, for a survey like Planck, masking clusters detected at high significance in the CMB maps themselves is not sufficient since the residual contribution from high-redshift, low-mass clusters below the detection threshold is still sizeable [184]. The power spectrum of residual thermal SZ emission may already have been seen by CBI [185] and BIMA [186] as an excess of observed small-scale power over that expected from the primary anisotropies. However, to reconcile the observed excess with SZ requires around twice the number density of clusters than predicted for standard cosmological parameters. Interestingly, recent data at the same frequency (30 GHz) from the Sunyaev-Zel'dovich Array [187] find no evidence for excess power after correction for the contribution of residual point sources. The origin of the discrepancy between these results is still unclear.

### 6.2.2. Doppler effects

Thomson scattering of CMB photons off free electrons in bulk flows after reionization generate frequency-independent temperature anisotropies

$$\Theta(\hat{\mathbf{n}}) = - \int an_e \sigma_T e^{-\tau} \hat{\mathbf{n}} \cdot \mathbf{v}_b d\eta, \quad (108)$$

via the Doppler effect. For an optical depth,  $\tau_{re} \sim 0.1$ , and r.m.s. peculiar velocities  $\sim 10^{-3}$ , the linear Doppler effect would swap the primary anisotropies were it not for a rather precise cancellation from integrating along the line of sight. The cancellation follows since  $\hat{\mathbf{n}} \cdot \mathbf{v}_b$  is the radial gradient of a potential in linear theory. The small net effect is shown in Fig. 11 and is at most two orders of magnitude below the power spectrum of the primary anisotropies.

Any spatial modulation of the electron density will tend to avoid the line-of-sight cancellation. This can arise from patchiness of the ionization fraction during reionization [188], or from the clumpiness of the (almost) fully-ionized intergalactic medium after reionization is complete [18, 20, 189]. Both effects produce anisotropies on scales of a few arcmin and below with the same thermal spectrum as the primary anisotropies. Computations of the power spectra of the modulated Doppler signals are shown in Fig. 11. The details of the patchy signal depend on the morphology of the ionized fraction (which affects where the power peaks) and the duration of reionization. Since the

physics of reionization is still rather uncertain, and calculating the anisotropies from patchy reionization properly requires large numerical simulations incorporating radiative transfer for the ionizing radiation, there remain significant modelling uncertainties in the predicted power spectrum.<sup>10</sup> However, the patchy signal is expected to be subdominant to the density-modulated Doppler signal. There are contributions to the latter from the linear density field (often called the Ostriker-Vishniac effect [20, 189]), which is easily calculated analytically, and from non-linear structures such as clusters of galaxies and filaments at low redshift (the kinetic Sunyaev-Zel'dovich effect [18]). The density-modulated Doppler signal is dominated by the non-linear effect on small scales ( $l > 1000$ ).

Observations of the small-scale temperature anisotropies can provide complementary information on reionization to that from large-angle polarization. In particular, the latter is mostly sensitive to the integrated optical depth  $\tau_{\text{re}}$ , with only weak sensitivity to the duration of reionization [60], and none to the morphology. By having one observing channel close to the null of the thermal Sunyaev-Zel'dovich effect, experiments like the South-Pole Telescope and the Atacama Cosmology Telescope should detect the power spectrum of the Doppler signals at very high significance [190].

Small-angle polarization generated at reionization should be around two orders of magnitude below the temperature signal generated there and will likely remain unobservable [191]. Note, however, that it is a further source of  $B$ -mode polarization.

## ACKNOWLEDGMENTS

AC thanks the organisers for the invitation to participate in what was an excellent summer school in a beautiful location. HVP was supported in part by Marie Curie grant MIRG-CT-2007-203314 from the European Commission, and by a STFC Advanced Fellowship. HVP thanks the Galileo Galilei Institute for Theoretical Physics for the hospitality and the INFN for partial support during the completion of this work.

## REFERENCES

1. R. Durrer, *The cosmic microwave background*, Cambridge University Press: Cambridge, UK, 2008.
2. G. F. Smoot et al., *ApJ* **396**, L1 (1992).
3. G. Hinshaw et al., *ApJS* **180**, 225 (2009).
4. The Planck Collaboration, *ArXiv Astrophysics e-prints* (2006), [astro-ph/0604069](https://arxiv.org/abs/astro-ph/0604069).
5. M. J. Rees, *ApJ* **153**, L1 (1968).
6. M. Zaldarriaga, *Phys. Rev. D* **55**, 1822 (1997).
7. J. M. Kovac, E. M. Leitch, C. Pryke, J. E. Carlstrom, N. W. Halverson, and W. L. Holzapfel, *Nature* **420**, 772 (2002).
8. L. Page et al., *ApJS* **170**, 335 (2007).
9. J. Dunkley et al., *ApJS* **180**, 306–329 (2009).
10. U. Seljak, and M. Zaldarriaga, *Phys. Rev. Lett* **78**, 2054 (1997).
11. M. Kamionkowski, A. Kosowsky, and A. Stebbins, *Phys. Rev. Lett.* **78**, 2058 (1997).

---

<sup>10</sup> The computation in Fig. 11 assumes a simple semi-analytic prescription for the growth and clustering of the ionized regions [188].

12. P. J. Steinhardt, and N. Turok, *Science* **296**, 1436 (2002).
13. N. Aghanim, S. Majumdar, and J. Silk, *Reports on Progress in Physics* **71**, 066902 (2008).
14. M. J. Rees, and D. W. Sciama, *Nature* **217**, 511 (1968).
15. A. Blanchard, and J. Schneider, *A&A* **184**, 1 (1987).
16. S. Cole, and G. Efstathiou, *MNRAS* **239**, 195 (1989).
17. A. Lewis, and A. Challinor, *Phys. Rep.* **429**, 1 (2006).
18. R. A. Sunyaev, and Y. B. Zeldovich, *Comments on Astrophysics and Space Physics* **4**, 173 (1972).
19. R. A. Sunyaev, and I. B. Zeldovich, *MNRAS* **190**, 413 (1980).
20. J. P. Ostriker, and E. T. Vishniac, *ApJ* **306**, L51 (1986).
21. W. Hu, and S. Dodelson, *ARA&A* **40**, 171 (2002).
22. W. Hu, *Annals of Physics* **303**, 203 (2003).
23. A. Challinor, "Cosmic Microwave Background Anisotropies," in *LNP Vol. 653: The Physics of the Early Universe*, edited by K. Tamvakis, 2005, p. 71.
24. J. C. Mather et al., *ApJ* **420**, 439 (1994).
25. D. J. Fixsen, and J. C. Mather, *ApJ* **581**, 817 (2002).
26. A. Kogut et al., *ApJ* **419**, 1 (1993).
27. L. Knox, *Phys. Rev. D* **52**, 4307 (1995).
28. G. Efstathiou, *MNRAS* **349**, 603 (2004).
29. M. R. Nolta et al., *ApJS* **180**, 296 (2009).
30. C. L. Reichardt et al., *ArXiv e-prints* (2008), 0801.1491.
31. W. C. Jones et al., *ApJ* **647**, 823 (2006).
32. W. Hu, *Phys. Rev. D* **64**, 083005 (2001).
33. P. J. E. Peebles, *ApJ* **153**, 1 (1968).
34. Y. B. Zeldovich, V. G. Kurt, and R. A. Syunyaev, *Zhurnal Eksperimental noi i Teoreticheskoi Fiziki* **55**, 278 (1968).
35. S. Seager, D. D. Sasselov, and D. Scott, *ApJS* **128**, 407 (2000).
36. W. A. Fendt, J. Chluba, J. A. Rubino-Martin, and B. D. Wandelt, *ArXiv e-prints* (2008), 0807.2577.
37. U. Seljak, and M. Zaldarriaga, *ApJ* **469**, 437 (1996).
38. A. Lewis, A. Challinor, and A. Lasenby, *ApJ* **538**, 473 (2000).
39. W. Hu, and N. Sugiyama, *ApJ* **444**, 489 (1995).
40. U.-L. Pen, U. Seljak, and N. Turok, *Phys. Rev. Lett.* **79**, 1611 (1997).
41. S. Dodelson, *Modern cosmology*, Academic Press: Amsterdam, 2008.
42. R. K. Sachs, and A. M. Wolfe, *ApJ* **147**, 73 (1967).
43. W. Hu, and M. White, *Phys. Rev. D* **56**, 596 (1997).
44. E. Komatsu et al., *ApJS* **180**, 330 (2009).
45. M. Zaldarriaga, and U. Seljak, *Phys. Rev. D* **55**, 1830 (1997).
46. M. Kamionkowski, A. Kosowsky, and A. Stebbins, *Phys. Rev. D* **55**, 7368 (1997).
47. V. Bozza, M. Gasperini, M. Giovannini, and G. Veneziano, *Phys. Lett. B* **543**, 14 (2002).
48. D. H. Lyth, C. Ungarelli, and D. Wands, *Phys. Rev. D* **67**, 023503 (2003).
49. D. Polarski, and A. A. Starobinsky, *Phys. Rev. D* **50**, 6123 (1994).
50. C. Gordon, D. Wands, B. A. Bassett, and R. Maartens, *Phys. Rev. D* **63**, 023506 (2001).
51. G. Efstathiou, and J. R. Bond, *MNRAS* **218**, 103 (1986).
52. R. Bean, J. Dunkley, and E. Pierpaoli, *Phys. Rev. D* **74**, 063503 (2006).
53. J. N. Goldberg, A. J. Macfarlane, E. T. Newman, F. Rohrlich, and S. E. C. G., *J. Math. Phys.* **8**, 2155 (1967).
54. A. Lewis, A. Challinor, and N. Turok, *Phys. Rev. D* **65**, 023505 (2002).
55. T. Okamoto, and W. Hu, *Phys. Rev. D* **66**, 063008 (2002).
56. W. Hu, and M. White, *New Astronomy* **2**, 323 (1997).
57. D. Coulson, R. G. Crittenden, and N. G. Turok, *Phys. Rev. Lett.* **73**, 2390 (1994).
58. A. Challinor, *Class. Quant. Grav.* **17**, 871 (2000).
59. A. Challinor, *Phys. Rev. D* **62**, 043004 (2000).
60. M. Kaplinghat, M. Chu, Z. Haiman, G. P. Holder, L. Knox, and C. Skordis, *ApJ* **583**, 24 (2003).
61. W. Hu, and G. P. Holder, *Phys. Rev. D* **68**, 023001 (2003).
62. X. Fan, M. A. Strauss, R. H. Becker, R. L. White, J. E. Gunn, G. R. Knapp, G. T. Richards, D. P. Schneider, J. Brinkmann, and M. Fukugita, *AJ* **132**, 117 (2006).

63. C. Pryke et al., *ApJ* **692**, 1247 (2009).
64. F. Piacentini et al., *ApJ* **647**, 833 (2006).
65. T. E. Montroy et al., *ApJ* **647**, 813 (2006).
66. E. M. Leitch, J. M. Kovac, N. W. Halverson, J. E. Carlstrom, C. Pryke, and M. W. E. Smith, *ApJ* **624**, 10 (2005).
67. C. Bischoff et al., *ApJ* **684**, 771 (2008).
68. J. L. Sievers et al., *ApJ* **660**, 976 (2007).
69. P. G. Castro et al., *ArXiv e-prints* (2009), 0901.0810.
70. G. Efstathiou, and J. R. Bond, *MNRAS* **304**, 75 (1999).
71. D. N. Spergel et al., *ApJS* **148**, 175 (2003).
72. J. Lesgourgues, and S. Pastor, *Phys. Rep.* **429**, 307 (2006).
73. A. H. Guth, *Phys. Rev. D* **23**, 347 (1981).
74. A. D. Linde, *Phys. Lett.* **B108**, 389 (1982).
75. A. Albrecht, and P. J. Steinhardt, *Phys. Rev. Lett.* **48**, 1220 (1982).
76. V. F. Mukhanov, H. A. Feldman, and R. H. Brandenberger, *Phys. Rep.* **215**, 203 (1992).
77. A. A. Starobinsky, *JETP Lett.* **30**, 682–685 (1979).
78. A. A. Starobinskii, *Soviet Ast. Lett.* **11**, 133 (1985).
79. V. Mukhanov, *Physical Foundations of Cosmology*, Cambridge University Press, Cambridge, UK, 2005.
80. W. H. Kinney, *ArXiv Astrophysics e-prints* (2009), 0902.1529.
81. A. R. Liddle, and D. H. Lyth, *Cosmological inflation and large-scale structure*, Cambridge University Press, Cambridge, UK, 2000.
82. D. H. Lyth, *Phys. Rev. Lett.* **78**, 1861 (1997).
83. D. Baumann, et al., *ArXiv Astrophysics e-prints* (2008), 0811.3919.
84. E. Silverstein, and A. Westphal, *ArXiv Astrophysics e-prints* (2008), 0803.3085.
85. L. McAllister, E. Silverstein, and A. Westphal, *ArXiv Astrophysics e-prints* (2008), 0808.0706.
86. D. Baumann, and L. McAllister, *ArXiv Astrophysics e-prints* (2009), 0901.0265.
87. D. Baumann, and H. V. Peiris, *ArXiv Astrophysics e-prints* (2008), 0810.3022.
88. D. N. Spergel, and M. Zaldarriaga, *Phys. Rev. Lett.* **79**, 2180 (1997).
89. H. V. Peiris, et al., *ApJS* **148**, 213 (2003).
90. M. Kowalski, et al., *ArXiv Astrophysics e-prints* (2008), 0804.4142.
91. W. J. Percival, et al., *MNRAS* **381**, 1053 (2007).
92. L. McAllister, E. Silverstein, and A. Westphal, *ArXiv Astrophysics e-prints* (2008), 0808.0706.
93. S. Kachru, et al., *JCAP* **0310**, 013 (2003).
94. D. Baumann, A. Dymarsky, I. R. Klebanov, L. McAllister, and P. J. Steinhardt, *Phys. Rev. Lett.* **99**, 141601 (2007).
95. D. Baumann, A. Dymarsky, I. R. Klebanov, and L. McAllister, *JCAP* **0801**, 024 (2008).
96. D. Baumann, A. Dymarsky, S. Kachru, I. R. Klebanov, and L. McAllister (2008).
97. J. P. Conlon, and F. Quevedo, *JHEP* **01**, 146 (2006).
98. J. J. Blanco-Pillado, et al., *JHEP* **09**, 002 (2006).
99. P. De Bernardis, M. Bucher, C. Burigana, and L. Piccirillo, *Experimental Astronomy* p. 45 (2008).
100. S. Chongchitnan, and G. Efstathiou, *Phys. Rev. D* **72**, 083520 (2005).
101. D. J. H. Chung, G. Shiu, and M. Trodden, *Phys. Rev. D* **68**, 063501 (2003).
102. M. Malquarti, S. M. Leach, and A. R. Liddle, *Phys. Rev. D* **69**, 063505 (2004).
103. R. Easther, and H. Peiris, *JCAP* **0609**, 010 (2006).
104. H. Peiris, and R. Easther, *JCAP* **0610**, 017 (2006).
105. G. Ballesteros, J. A. Casas, and J. R. Espinosa, *JCAP* **0603**, 001 (2006).
106. P. Adshead, and R. Easther, *ArXiv Astrophysics e-prints* (2008), 0802.3898.
107. M. Sasaki, and E. D. Stewart, *Prog. Theor. Phys.* **95**, 71 (1996).
108. J. Silk, and M. S. Turner, *Phys. Rev. D* **35**, 419 (1987).
109. R. Holman, E. W. Kolb, S. L. Vadas, and Y. Wang, *Phys. Lett. B* **269**, 252 (1991).
110. D. Polarski, and A. A. Starobinsky, *Nucl. Phys. B* **385**, 623 (1992).
111. D. H. Lyth, and E. D. Stewart, *Phys. Rev. D* **53**, 1784 (1996).
112. C. P. Burgess, R. Easther, A. Mazumdar, D. F. Mota, and T. Multamaki, *JHEP* **05**, 067 (2005).
113. A. A. Starobinsky, *JETP Lett.* **55**, 489 (1992).
114. J. A. Adams, B. Cresswell, and R. Easther, *Phys. Rev. D* **64**, 123514 (2001).

115. L. Covi, J. Hamann, A. Melchiorri, A. Slosar, and I. Sorbera, *Phys. Rev. D* **74**, 083509 (2006).
116. J. Hamann, L. Covi, A. Melchiorri, and A. Slosar, *Phys. Rev. D* **76**, 023503 (2007).
117. P. Hunt, and S. Sarkar, *Phys. Rev. D* **70**, 103518 (2004).
118. P. Hunt, and S. Sarkar, *Phys. Rev. D* **76**, 123504 (2007).
119. X. Chen, *Phys. Rev. D* **71**, 063506 (2005).
120. X. Chen, *JHEP* **08**, 045 (2005).
121. R. Bean, X. Chen, H. V. Peiris, and J. Xu, *Phys. Rev. D*, 023527 (2008).
122. H. V. Peiris, and R. Easther, *ArXiv Astrophysics e-prints* (2008), 0805.2154.
123. S. Hawking, *MNRAS* **152**, 75 (1971).
124. B. J. Carr, and S. W. Hawking, *MNRAS* **168**, 399 (1974).
125. B. J. Carr, J. H. Gilbert, and J. E. Lidsey, *Phys. Rev. D* **50**, 4853 (1994).
126. H. I. Kim, and C. H. Lee, *Phys. Rev. D* **54**, 6001 (1996).
127. A. M. Green, and A. R. Liddle, *Phys. Rev. D* **56**, 6166 (1997).
128. L. Covi, and D. H. Lyth, *Phys. Rev. D* **59**, 063515 (1999).
129. J. Yokoyama, *Prog. Theor. Phys. Suppl.* **136**, 338 (1999).
130. S. M. Leach, I. J. Grivell, and A. R. Liddle, *Phys. Rev. D* **62**, 043516 (2000).
131. I. Zaballa, A. M. Green, K. A. Malik, and M. Sasaki, *JCAP* **0703**, 010 (2007).
132. S. Chongchitnan, and G. Efstathiou, *JCAP* **0701**, 011 (2007).
133. K. Kohri, D. H. Lyth, and A. Melchiorri, *JCAP* **0804**, 038 (2008).
134. A. D. Linde, *Phys. Lett. B* **175**, 395 (1986).
135. B. G. Keating, C. W. O'Dell, A. de Oliveira-Costa, S. Klawikowski, N. Stebor, L. Piccirillo, M. Tegmark, and P. T. Timbie, *ApJ* **560**, 1 (2001).
136. G. Efstathiou, S. Gratton, and F. Paci, *ArXiv e-prints* (2009), 0902.4803.
137. K. W. Yoon et al., *SPIE* **6275**, 51 (2006).
138. C. E. North et al., *ArXiv e-prints* (2008), 0805.3690.
139. D. Samtleben et al., *ArXiv e-prints* (2008), 0806.4334.
140. R. Charlassier et al., *ArXiv e-prints* (2008), 0805.4527.
141. P. Oxley et al., *SPIE*, **5543**, 320 (2004).
142. B. P. Crill et al., *SPIE*, **7010**, 79 (2008).
143. W. Hu, *Phys. Rev. D* **65**, 023003 (2002).
144. W. Hu, and T. Okamoto, *ApJ* **574**, 566 (2002).
145. L. Verde, H. V. Peiris, and R. Jimenez, *JCAP* **1**, 19 (2006).
146. J. Dunkley et al., *ArXiv e-prints* (2008), 0811.3915.
147. J. Maldacena, *JHEP* **5**, 13 (2003).
148. N. Bartolo, E. Komatsu, S. Matarrese, and A. Riotto, *Phys. Rep.* **402**, 103 (2004).
149. X. Chen, M.-x. Huang, S. Kachru, and G. Shiu, *JCAP* **0701**, 002 (2007).
150. J. R. Fergusson, and E. P. S. Shellard, *ArXiv Astrophysics e-prints* (2008), 0812.3413.
151. A. D. Linde, and V. F. Mukhanov, *Phys. Rev. D* **56**, 535 (1997).
152. D. Babich, P. Creminelli, and M. Zaldarriaga, *JCAP* **0408**, 009 (2004).
153. R. Holman, and A. J. Tolley, *JCAP* **0805**, 001 (2008).
154. X. Chen, R. Easther, and E. A. Lim, *JCAP* **0706**, 023 (2007).
155. N. Bartolo, S. Matarrese, and A. Riotto, *JCAP* **5**, 10 (2006).
156. N. Bartolo, S. Matarrese, and A. Riotto, *JCAP* **6**, 24 (2006).
157. N. Bartolo, S. Matarrese, and A. Riotto, *JCAP* **0701**, 19 (2007).
158. C. Pitrou, J.-P. Uzan, and F. Bernardeau, *Phys. Rev. D* **78**, 063526 (2008).
159. L. Senatore, S. Tassev, and M. Zaldarriaga, *ArXiv e-prints* (2008), 0812.3652.
160. C. Pitrou, *Class. Quant. Grav.* **26**, 065006 (2009).
161. D. Nitta, E. Komatsu, N. Bartolo, S. Matarrese, and A. Riotto, *ArXiv e-prints* (2009), 0903.0894.
162. L. Wang, and M. Kamionkowski, *Phys. Rev. D* **61**, 063504 (2000).
163. E. Komatsu, and D. N. Spergel, *Phys. Rev. D* **63**, 063002 (2001).
164. K. M. Smith, L. Senatore, and M. Zaldarriaga, *ArXiv e-prints* (2009), 0901.2572.
165. J. T. L. Zwart et al., *MNRAS* **391**, 1545 (2008).
166. S. Muchovej et al., *ApJ* **663**, 708 (2007).
167. J. Ruhl et al., *SPIE* **5498**, 11 (2004).
168. A. Kosowsky, *New Astronomy Review* **50**, 969 (2006).
169. J. Weller, and A. M. Lewis, *MNRAS* **346**, 987 (2003).

170. R. G. Crittenden, and N. Turok, *Phys. Rev. Lett.* **76**, 575 (1996).
171. S. Boughn, and R. Crittenden, *Nature* **427**, 45 (2004).
172. T. Giannantonio, R. Scranton, R. G. Crittenden, R. C. Nichol, S. P. Boughn, A. D. Myers, and G. T. Richards, *Phys. Rev. D* **77**, 123520 (2008).
173. S. Ho, C. Hirata, N. Padmanabhan, U. Seljak, and N. Bahcall, *Phys. Rev. D* **78**, 043519 (2008).
174. U. Seljak, *ApJ* **460**, 549 (1996).
175. M. Zaldarriaga, and U. Seljak, *Phys. Rev. D* **58**, 023003 (1998).
176. K. M. Smith et al., *ArXiv e-prints* (2008), 0811.3916.
177. W. Hu, *ApJ* **557**, L79 (2001).
178. K. M. Smith, O. Zahn, and O. Doré, *Phys. Rev. D* **76**, 043510 (2007).
179. C. M. Hirata, S. Ho, N. Padmanabhan, U. Seljak, and N. A. Bahcall, *Phys. Rev. D* **78**, 043520 (2008).
180. D. Munshi, P. Valageas, L. van Waerbeke, and A. Heavens, *Phys. Rep.* **462**, 67 (2008).
181. M. Birkinshaw, *Phys. Rep.* **310**, 97–195 (1999).
182. Z. Staniszewski et al., *ArXiv e-prints* (2008), 0810.1578.
183. J. Weller, R. A. Battye, and R. Kneissl, *Phys. Rev. Lett.* **88**, 231301 (2002).
184. N. Taburet, N. Aghanim, M. Douspis, and M. Langer, *MNRAS* **392**, 1153 (2009).
185. J. L. Sievers et al., *ArXiv e-prints* (2009), 0901.4540.
186. K. S. Dawson, W. L. Holzapfel, J. E. Carlstrom, M. Joy, and S. J. LaRoque, *ApJ* **647**, 13 (2006).
187. M. K. Sharp et al., *ArXiv e-prints* (2009), 0901.4342.
188. A. Gruzinov, and W. Hu, *ApJ* **508**, 435 (1998).
189. E. T. Vishniac, *ApJ* **322**, 597 (1987).
190. O. Zahn, M. Zaldarriaga, L. Hernquist, and M. McQuinn, *ApJ* **630**, 657 (2005).
191. W. Hu, *ApJ* **529**, 12 (2000).